Modeling of martensitic phase transformation. Numerics, microstructure and applications.

Issa, Sally

2026

Document Version:
Publisher's PDF, also known as Version of record

LUND UNIVERSITY

MODELING OF MARTENSITIC PHASE TRANSFORMATION NUMERICS, MICROSTRUCTURES AND APPLICATIONS

SALLY ISSA

Solid Mechanics

Doctoral Thesis

Department of Construction Sciences
Solid Mechanics

ISRN: LUTFD2/TFHF-26/1075-SE(1–180)
ISBN: 978-91-90202-67-8 (print)
ISBN: 978-91-90202-68-5 (PDF)

Modeling of martensitic phase transformation
Numerics, microstructures and applications

Doctoral Thesis by

Sally Issa

Printed by Media-Tryck AB, Lund, Sweden
For information, address:
Division of Solid Mechanics, Lund University, Box 118, SE-221 00 Lund, Sweden
Homepage: `www.solid.lth.se`

To my children

Hashem, Yafa & Rima Falastin

May you always have the courage to follow your dreams, the patience to overcome challenges and the confidence to believe in yourself

Preface

The work presented in this thesis began in September 2011 during my employment at the Division of Solid Mechanics. Although my employment ended in December 2017, the work on this thesis continued in the years that followed. Throughout this journey, life brought both challenges and joys. I lost my father and later I met my husband. I faced challenges in the research and had to reorganize my PhD plans. What started as my first project had to be postponed and put aside and it ended up becoming my third article.

I moved to another country in the years that followed, built a new life, became a mother of three children and worked in different companies. All while carrying with me the unfinished goal of completing this thesis. For many years, this thesis was always in the back of my mind, even during periods when I could not dedicate any real time to it. There were times when I wondered if I would ever finish it. Today, as I write these final words, I feel that a dream I carried with me for many years has finally become a reality.

I would like to express my deep gratitude to my supervisors, Mathias Wallin, Håkan Hallberg and Matti Ristinmaa. Thank you for your guidance, support and patience throughout this long journey. Without your support and the knowledge you shared with me, I would not be here.

I would also like to thank my family, especially my mother and my husband who never stopped reminding me that I had to finish what I started. Their support and belief in me helped me continue, even during the times when completing this thesis seemed far away. I am also grateful to my friends, both those who believed in me and those who did not. To those who encouraged me, thank you for your support. To those who doubted me, thank you as well. Your doubts gave me an extra reason to keep going and prove that I could do it.

This thesis is much more than an academic achievement for me. It represents a promise I made to myself many years ago. It has taught me that goals can still be reached, even when life takes you in completely different directions and the journey becomes much longer than expected. It has taught me patience and humility. Most of all, it has taught me that life does not always follow the plans we make and that sometimes we need to adapt, take a different route and keep moving forward. I am proud to have finally completed this work and to close this chapter of my life.

Barcelona, June 2026
Sally Issa

Abstract

This thesis investigates the martensitic phase transformation with the aim of developing predictive models for its formation and evolution under different conditions. The work seeks to provide a fundamental understanding of martensitic transformation through both macroscale continuum modeling and mesoscale crystal plasticity modeling.

The continuum modeling considers the austenite to martensite phase transformation coupled to large strain plasticity and is formulated to capture the rate dependence of plastic deformation during laser shock peening. The model is used to identify the relative influence of process parameters on the formation of martensite and plastic deformation and is further applied to study the influence of martensitic transformation on crack propagation. It is shown that, under certain conditions, the martensitic phase transformation can retard crack propagation.

The crystal plasticity model, on the other hand, is employed to investigate lath martensite and the effect of block boundaries on the macroscopic strength of the material. Block boundaries are shown to act as obstacles to dislocation motion, which contributes to the strengthening mechanism. In addition, a numerical study of the crystal plasticity formulation is conducted, in which a diagonally implicit Runge-Kutta method is evaluated as a solution scheme.

The proposed modeling framework and numerical methods contribute to an improved understanding of martensitic transformation and support the design of metallic materials with enhanced performance for advanced engineering applications.

Popular science summary

Metals consist of one or several phases, where each phase is a region in which atoms are arranged in a consistent way, giving the material uniform properties throughout the phase. Phase transformations can be triggered by external influences such as deformation and may lead to changes in the overall behavior, such as increased strength.

A key transformation studied in this thesis is the martensitic phase transformation. This transformation occurs when the austenite phase rapidly changes into martensite without atomic diffusion, meaning that atoms shift collectively rather than moving over long distances. The martensitic phase is harder and stronger than austenite, but also more brittle. By controlling when and how this transformation occurs, it is possible to tailor the mechanical properties of the material. Martensitic transformation is most commonly found in steels but can also occur in other alloy systems such as nickel-, copper-, and titanium-based alloys.

This thesis focuses on understanding and modeling how martensitic transformation forms and evolves under different conditions. It uses mathematical descriptions to model how the material responds to forces and deformation. These models are implemented in computer simulations that can predict the behavior of the material.

Applications of these concepts are studied in this thesis. For example, in laser shock peening, where the material is subjected to very rapid deformation, martensite near the surface forms and increases the surface hardness. Similarly, during crack propagation, the material can undergo martensitic transformation at the crack tip. This transformation absorbs energy and can slow down crack growth, thereby improving the toughness of the material.

Another important aspect of this thesis is the development of numerical methods to simulate the material behavior. This includes how the mathematical models are solved efficiently and accurately to capture the underlying physical mechanisms. Together, these approaches contribute to a better understanding of martensitic transformation and support the design of materials with improved performance for advanced engineering applications.

Populärvetenskaplig sammanfattning

Metaller består av en eller flera faser, där varje fas utgör ett område med en väldefinierad atomstruktur och därmed homogena egenskaper. Fasomvandlingar kan induceras av externa faktrorer så som deformation och kan leda till förändringar i materialets makroskopiska beteende, exempelvis dess hållfasthet.

Denna avhandling undersöker den så kallade martensitiska fasomvandlingen. Denna omvandling innebär att austenitfasen snabbt omvandlas till martensit utan diffusion, vilket betyder att atomerna förskjuts gemensamt i stället för att förflytta sig över längre avstånd. Martensit är hårdare och starkare än austenit, men också mer spröd. Genom att styra när och hur denna omvandling sker kan materialets mekaniska egenskaper anpassas. Denna fasomvandling är vanligast i stål men förekommer även i andra legeringssystem, till exempel nickel-, koppar- och titanbaserade legeringar.

Forskningen som presenteras i denna avhandling syftar till att modellera hur martensitisk omvandling initieras och utvecklas under olika förhållanden. Matematiska modeller används för att beskriva hur materialet reagerar på belastning och deformation, och dessa implementeras i numeriska simuleringar för att förutsäga materialets beteende.

Tillämpningar av martensit omvandlingen som studeras i denna avhandling är ytbehandlingar med laser, där materialet utsätts för mycket snabba deformationer. Detta kan inducera martensitbildning nära ytan, vilket ökar ythårdheten och förbättrar materialets prestanda. På liknande sätt kan martensitisk omvandling uppstå vid sprickspetsen under spricktillväxt, där höga spänningar råder. Fasomvandlingen kan då absorbera energi och därigenom bromsa sprickans tillväxt, vilket ökar materialets seghet.

En annan central del av arbetet är utvecklingen av numeriska metoder för att simulera materialbeteende. Detta innefattar effektiva och noggranna lösningsmetoder för de matematiska modellerna, så att de relevanta fysikaliska mekanismerna kan återges. Sammantaget bidrar resultaten till en fördjupad förståelse av martensitisk omvandling och ger underlag för utveckling av material med förbättrade egenskaper för avancerade ingenjörstillämpningar.

Contents

Chapter 1

Introduction

The martensitic phase transformation has been known since the late 19th century where it was first characterized during the study of the microstructure of hardened steel by the German metallographer Adolf Martens. Since then, this transformation has been studied extensively and has become one of the most important solid-solid phase transformations, finding a wide range of applications in material science and engineering. This transformation is a crucial strengthening mechanism in steels and other alloys, as well as it being the basis for the shape memory effect and superelasticity observed in shape memory alloys. It plays an essential role in many advanced high-strength steels, including dual-phase steels and transformation-induced plasticity steels. It is utilized in diverse fields ranging from aerospace and biomedical engineering to automotive and civil infrastructure [1, 2].

Experimental studies of martensitic phase transformation performed using in-situ bulk techniques such as synchrotron X-ray and neutron diffraction, together with microscopy techniques such as Transmission electron microscopy (TEM) and Electron backscatter diffraction, or a combination of these bulk diffraction and local microscopy techniques have revealed critical details about the transformation mechanisms. It is shown that martensite often forms through multistage transformation $\gamma \rightarrow \varepsilon \rightarrow \alpha'$ and it has been possible to track the transformation in real time and at grain level, confirming when and where intermediate ε-martensite forms and how it subsequently transforms to α'-martensite. It is also shown that transformation strongly depends on grain orientation and size as well as the surrounding microstructure. Through grain-resolved measurments, it has been possible to demonstrate that certain austenite grains transform preferentially depending on their crystallographic orientation and local stress state. Computational modeling is important as it integrates data obtained from different experimental techniques into a coherent mechanistic framework. Furthermore, it enables the prediction of macroscopic mechanical properties

based on microstructural observations, allows testing of hypotheses that cannot be isolated experimentally and supports the inverse design of processing routes to tailor martensite morphology and properties [3–6].

Nevertheless, despite significant advances in multiscale modeling of martensitic transformation, several critical aspects remain insufficiently studied. Specifically, numerical models capable of capturing the influence of process parameters during surface treatments on martensitic phase transformation are lacking. This aspect is addressed in Paper A. Furthermore, the effects of phase transformations on crack propagation behavior require advanced modeling approaches, which are investigated in Paper B. Additionally, the development of robust and efficient numerical algorithms remains important, and this is explored in Paper C. The aim of this thesis is to provide an understanding of martensitic phase transformations through numerical modeling, with a focus on microstructure evolution and applications. In the next sections the fundamentals of crystalline material structure as well as the fundamentals of martensitic phase transformation will be outlined. Then, the basics of constitutive modeling used to simulate crystal material behavior, along with phase transformation, will be presented. This will provide a comprehensive understanding of the modeling and computational tools used to study and predict the behavior of martensitic materials.

Chapter 2

The structure of crystalline solids

To understand martensitic phase transformation, it is first necessary to examine how atoms are organized in the solid state. In crystalline materials, atoms are arranged in a periodic lattice exhibiting long-range order. This arrangement can be described by a three-dimensional space lattice with the unit cell as the smallest repeating element capturing the symmetry of the structure. The unit cell is typically a parallelepiped with the lattice parameters a, b and c and the interaxial angles α, β and γ. These are indicated in Fig. 2.1(a).

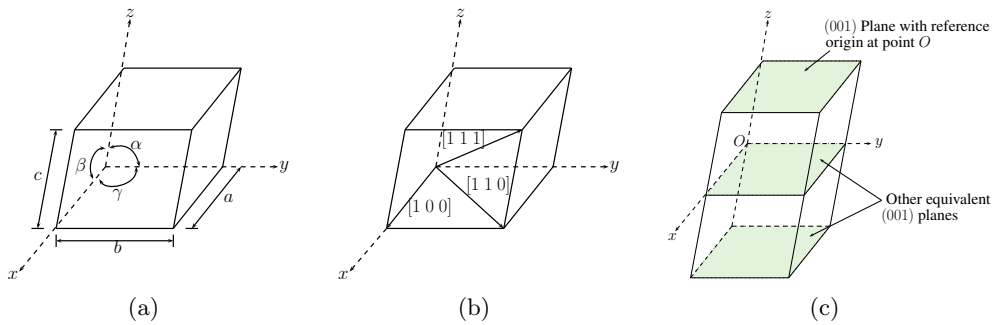

Figure 2.1: (a) Schematic of a unit cell showing its lattice parameters and crystal axes. (b) Illustration of crystallographic directions represented as vectors in the lattice, using Miller indices $[uvw]$. (c) Representation of crystallographic planes within the unit cell, indexed using Miller indices (hkl).

An important concept when describing crystalline materials is specifying crystallographic direction and planes. Directions are expressed using Miller index notation in square brackets $[uvw]$, where u, v and w are the vector components along the unit cell axes, reduced to the smallest integer ratio, e.g. [100] and

[110], see Fig. 2.1(b). Similarly, crystallographic planes are denoted by Miller indices (hkl) obtained from the reciprocals of the intercepts with the crystallographic axes. Parallel planes share identical indices and symmetry equivalent planes form families denoted by $\{hkl\}$, such as $\{001\}$ in cubic system, see Fig. 2.1(c). Negative intercepts are indicated with a bar. In the same way, $\langle uvw \rangle$ represents families of equivalent directions, for example $\langle 100 \rangle$.

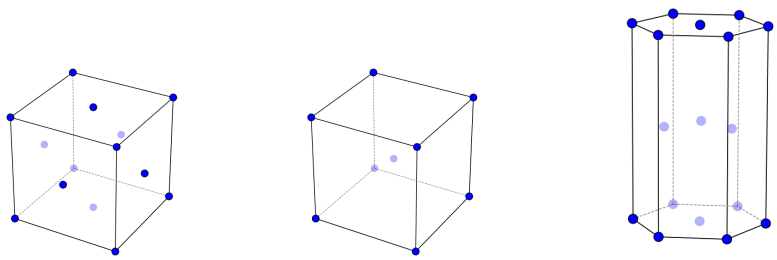

(a) (b) (c)

Figure 2.2: Visualization of the three crystal structures: (a) FCC, (b) BCC and (c) HCP. Front facing atoms are shown as opaque small circles, while back facing atoms are transparent small circles. Solid lines indicate front-facing edges and dashed lines represent back-facing edges.

Crystal structures are classified into seven systems: cubic, tetragonal, hexagonal, trigonal, orthorhombic, monoclinic and triclinic, based on lattice parameters and interaxial angles. Most metals adopt three common structures: Face Centered Cubic (FCC) with atoms at cube corners and face centers, Body Centered Cubic (BCC) with atoms at the corners and one atom at the cube center and Hexagonal Close-Packed (HCP) consisting of hexagonal layers with an additional mid-plane of atoms. In Fig. 2.2 (a)-(c), the FCC, BCC and HCP crystal structures, are illustrated, respectively.

From a stacking perspective, FCC and HCP are close-packed, minimizing free volume where FCC follows an ABCABC sequence and HCP exhibits ABAB stacking. In contrast, BCC is not close-packed, with a less efficient atomic packing. In Fig. 2.3, an illustration of the ABCABC and the ABAB stacking sequences are shown. Likewise, crystallographic planes can be classified by packing density. In FCC, the $\{111\}$ planes are close-packed, with $\langle 110 \rangle$ directions as close-packed directions, whereas other planes such as $\{100\}$ and $\{110\}$ are not close-packed, despite belonging to a close-packed structure.

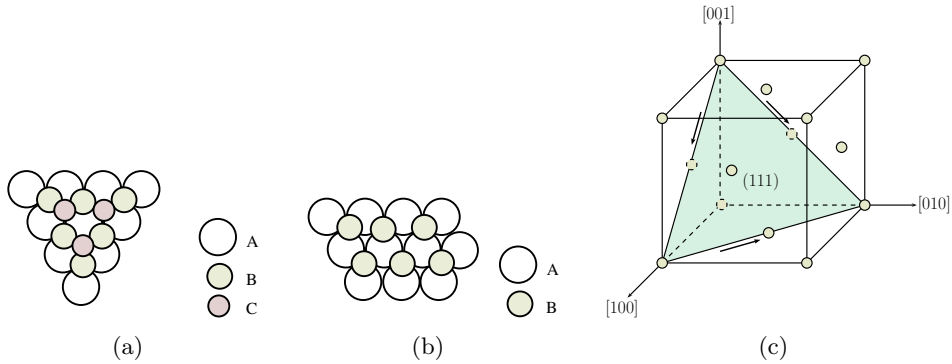

Figure 2.3: Schematic illustration of stacking sequences: (a) ABCABC, (b) ABAB and (c) an FCC unit cell showing the close-packed plane (111) with the corresponding close-packed directions ⟨110⟩ indicated with arrows.

While an ideal crystal is described by a periodic unit cell, most materials are polycrystalline, comprising grains with distinct crystallographic orientations. The interfaces separating neighboring grains are known as grain boundaries. These boundaries form during solidification as independently nucleated crystals come into contact, creating interfaces characterized by lattice mismatch and higher interfacial energy due to disrupted bonding. Depending on the misorientation, boundaries are classified as low- or high-angle. Fig. 2.4 shows a tilt grain boundary which arise from rotation about an axis lying in the boundary plane, whereas twist boundaries involve rotation about an axis normal to the plane. Most boundaries are mixed, combining both tilt and twist components [1, 7, 8].

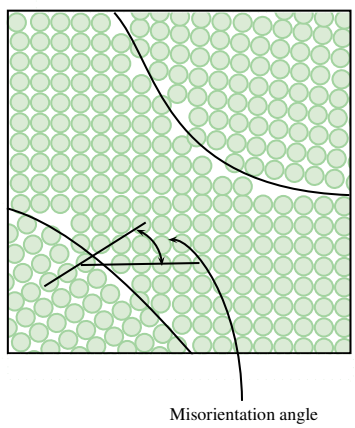

Figure 2.4: Grain boundary illustrated using a bubble model, showing the misorientation between adjacent grains and the resulting atomic disorder in the boundary region. The angle of misalignment between grains is also indicated.

2.1 Crystal defects

Grain boundaries are only one of several types of defects found in crystalline materials. Imperfections alter local atomic arrangements and bonding and are commonly categorized into point, line and planar defects, each affecting material behavior differently. Point defects, such as vacancies and interstitials, disrupt local atomic packing and influence diffusion. Line defects, or dislocations, typically classified as edge or screw types, are one-dimensional imperfections whose motion under stress governs plastic deformation. Planar defects, including grain boundaries and stacking faults are two-dimensional interfaces separating regions of different crystallographic orientation or stacking sequence. These defects are associated with high-energy regions and can significantly influence phase transformations by providing preferential nucleation sites and affecting transformation kinetics.

2.2 Deformation of crystals

Dislocations govern plastic deformation through their motion producing slip, which is the displacement of atomic planes along preferred crystallographic directions on densely packed planes. In FCC crystals, slip occurs on $\{111\}$ planes along $\langle 110 \rangle$ directions, resulting in 12 slip systems. Meanwhile, BCC crystals lack truly close-packed planes, thus slip primarily occurs on $\{110\}$ planes along $\langle 111 \rangle$ directions, resulting in 12 slip systems with additional activity on $\{112\}$ and $\{123\}$ slip planes at elevated temperatures and strain rates.

Once slip is activated, plastic deformation proceeds by relative lattice motion across slip planes while the regions between them primarily accommodate elastic deformation. Further deformation occurs by continued slip on active planes or activation of additional systems. As illustrated in Fig. 2.5, for a cylindrical single crystal under tensile loading, the slip plane normal and the slip direction form angles ϕ and λ with the tensile axis, respectively, which do not necessarily sum 90°. The resolved shear stress τ_{RSS} is given by Schmid's law as

$$\tau_{RSS} = \sigma \cos\phi \cos\lambda, \tag{2.1}$$

where σ is the applied normal stress. The slip initiates when τ_{RSS} on a given slip system exceeds the critical resolved shear stress τ_{CRSS} which is required to activate dislocation motion.

Slip system activity depends on crystal structure. FCC crystals, like aluminum and copper, have a relatively low τ_{CRSS} enabling high ductility, while BCC crystals exhibit higher τ_{CRSS}. HCP crystals generally have fewer active slip systems than FCC crystals, limiting their ductility. The crystallographic

nature of slip also forms the basis of crystal plasticity, in which plastic deformation is described by the evolution of slip on individual crystallographic slip systems. This framework is employed in Paper C.

In addition to dislocations, plastic deformations may also involve the formation of stacking faults and deformation twins. A stacking fault is a planar defect resulting from a local disruption of the close-packed stacking sequence. In FCC crystals with the sequence ABCABC, two types of stacking fault may form: intrinsic or extrinsic corresponding to the sequences ABCBCAB or ABACABC, respectively. The associated stacking fault energy influences the formation of stacking faults and the overall plastic response.

Deformation twinning represents another important mechanism of plastic deformation. During twinning, a twin boundary is formed. This special type of grain boundary is characterized by minor lattice symmetry across the twin plane, resulting in a crystallographic reorientation of the lattice, see Fig. 2.6(a). Twin boundaries form either by shear, so called mechanical twins, or during post-deformation annealing, giving so called annealing twins. Similar to slip, twinning occurs on specific planes and directions. However, slip preserves lattice orientation across the plane and produces discrete surface steps, whereas twinning induces a homogeneous shear with lattice reorientation, see Fig. 2.6(b). Although twinning contributes less to overall strain, it can facilitate further deformation by activating additional slip systems [1, 8–10].

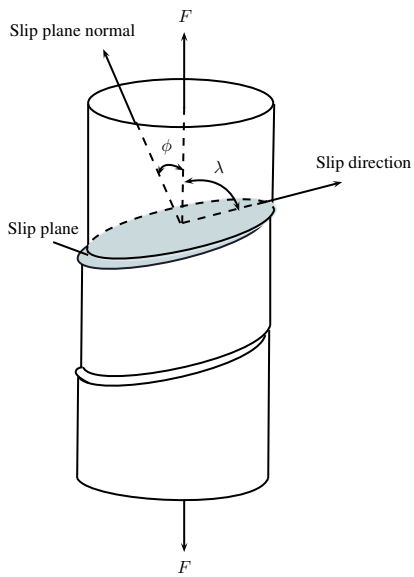

Figure 2.5: Illustration of the slip geometry in a cylindrical crystal. Note that, in general, $\phi + \lambda \neq 90^\circ$.

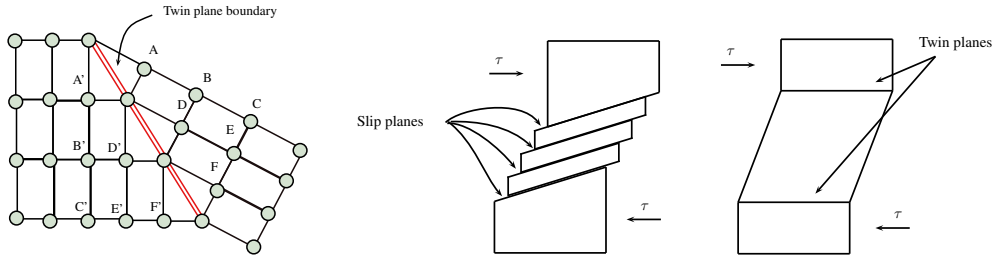

Figure 2.6: (a) Illustration of a twin plane and the adjacent atom positions. Atoms labeled with corresponding primed and unprimed letters occupy mirror symmetric positions across the twin plane. (b) Comparison of deformation by slip and deformation by twinning. The slip involves the shear displacement of atomic planes, while the twinning results in reorientation of the crystal lattice across a mirror-like twin boundary.

2.3 Crystallographic texture

The crystallographic orientation of a grain defines the spatial relationship between its crystal lattice and a fixed sample reference frame. In polycrystalline materials, the distribution of grain orientations is referred to as the crystallographic texture. Following solidification, grains are generally randomly oriented, resulting in a random texture and, consequently, nearly isotropic macroscopic behavior despite the anisotropy of individual crystals. However, thermomechanical processing, such as rolling, extrusion or forging, as well as certain phase transformations, can alter grain orientations through crystal rotation and lattice reorientation, giving rise to a preferred crystallographic texture. This preferred texture influences macroscopic properties including anisotropy, ductility, fatigue resistance and phase transformation kinetics.

Texture is commonly quantified by describing grain orientations relative to the sample frame using Bunge Euler angles (ϕ_1, Φ, ϕ_2), corresponding to sequential rotations about z-axis, rotated x-axis and the new z-axis. Together, these angles uniquely define the grain orientation enabling statistical analysis and modeling of texture evolution [1, 8, 11, 12].

2.4 Crystal strengthening mechanisms

In crystalline materials, strength is governed by resistance to plastic deformation, primarily through mechanisms that hinder dislocation motion. A key mechanism is grain boundary strengthening, known as Hall-Petch strengthening. Grain boundaries act as barriers to dislocation motion. As dislocations approach a boundary, they must change slip plane and direction to continue

into the adjacent grain. This transition becomes more difficult with increasing misorientation, particularly for high-angle boundaries. As a result, dislocations tend to pile up creating localized stress concentrations that can activate dislocation sources in neighboring grains. Consequently, decreasing grain size increases boundary density and enhances strength. This relationship is expressed by the phenomenological Hall-Petch equation

$$\sigma_y = \sigma_0 + \frac{k}{\sqrt{d}}, \tag{2.2}$$

where σ_y is the yield stress, σ_0 is the stress required to move dislocations, k is the strengthening constant and d is the average grain diameter [13]. In Paper D, the Hall-Petch relationship is employed to model strengthening in lath martensite.

Another strengthening mechanism is strain hardening, known as work hardening. During plastic deformation, dislocation density increases and their interactions form entanglements and dislocation forests that impede further motion. These interactions raise the stress required for continued glide and thus increase the yield strength.

Additional composition related strengthening mechanisms include solid solution strengthening, where solute atoms distort the crystal lattice and hinder dislocation motion, and precipitation strengthening, where dispersed second phase particles obstruct dislocation glide [1, 9, 11, 14]. Another important mechanism is strengthening through phase transformations. The formation of a new phase alters the crystal structure and introduces phase boundaries, transformation strains and local stress fields that hinder dislocation motion and increase the material strength. A prime example is martensitic transformation, the main focus of this thesis, which is addressed in the following section.

Chapter 3

Phase transformation

An understanding of phases and basic thermodynamic principles is essential for describing martensitic phase transformation. The stability of a crystal structure is governed by free energy and external conditions, thus phase transformation occurs when a change in these conditions alters the stability of a phase. The following section introduces fundamental concepts used to analyze martensitic transformation.

3.1 The concept of solid state phases

A phase refers to a distinct and identifiable state of matter. In a material, it is a region containing a large number of atoms, ions or molecules, separated from other regions by a bounding interface. A pure metal is therefore considered a single phase, even in the presence of grain boundaries or crystal defects. Phase diagrams provide a concise description of phase stability as a function of temperature, pressure and composition.

The iron-carbon phase diagram illustrated in Fig. 3.1 is one of the most important phase diagrams and is typically shown up to 6.7 wt.% carbon at 1 atm, since steels and cast irons lie below this limit. At 6.7 wt.% carbon, the intermediate compound iron carbide, or cementite (Fe_3C), forms, represented by the rightmost boundary.

Along the pure iron axis, iron undergoes successive phase transformations before melting. At room temperature, BCC α-ferrite transforms into FCC γ-austenite at 912°C. A second transformation occurs at 1394°C where γ-austenite transforms into BCC δ-ferrite before melting at 1538°C.

Carbon is an interstitial element in iron and forms a solid solution with α- and δ-ferrite as well as γ-austenite. In BCC α-ferrite, carbon solubility is very limited, with a maximum of 0.022 wt.% at 727°C, due to the restricted

interstitial space of the BCC lattice. Despite its low concentration, carbon strongly influences the mechanical properties of ferrite.

At 727°C and 0.76 wt.% carbon, the eutectoid point is reached, where austenite is in equilibrium with ferrite and cementite. At this composition, the eutectoid reaction occurs, in which austenite transforms into lamellar texture of ferrite and cementite. Austenite is stable above this temperature and can dissolve up to 2.14 wt.% carbon, reflecting the larger interstitial sites available in the FCC lattice compared with the BCC lattice. In contrast, δ-ferrite is stable only at high temperatures and has limited technological importance. Cementite is a hard and brittle intermetallic compound that contributes significantly to the strength and hardness of steels [1, 15, 16].

The phase diagram represents the thermodynamically stable phases for a given temperature and composition, assuming sufficient time for diffusion and equilibrium. However, martensite is a metastable phase and does not appear in the phase diagram, as it forms through a rapid displacive process rather than diffusion. The following section introduces the kinetic nature of martensitic transformation, providing the basis for understanding the formation of martensite.

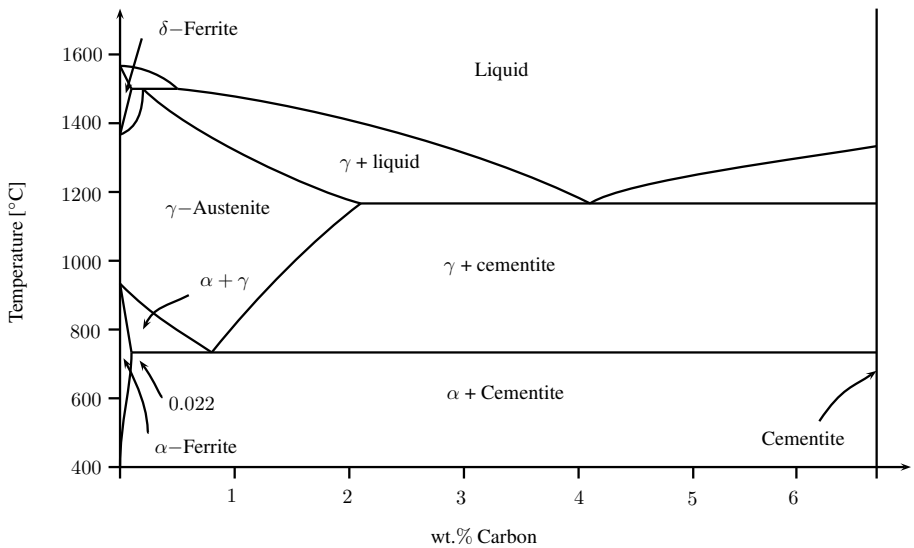

Figure 3.1: Schematic iron-carbon phase diagram.

3.2 Thermodynamic framework

For any given material, local equilibrium corresponds to the state in which each phase minimizes its free energy, determined by composition, temperature and pressure. The Gibbs phase rule at constant pressure, $P + F = C + 1$, defines the degrees of freedom in a multi-phase system where P is the number of phases present at equilibrium, F is the number of degrees of freedom and C is the number of components. At the eutectoid point in the Fe-C diagram, $P = 3$ and $C = 2$, giving $F = 0$, corresponding to an invariant state.

While the phase rule defines the number of independent variables, phase stability is governed by the Gibbs free energy, $G = H - TS$, which combines enthalpy, H, and the entropy, S, of the system and T is the absolute temperature. At constant temperature and pressure, equilibrium corresponds to the minimum G, and coexistence requires equal free energies of the phases.

Phase transformations depend on whether atomic diffusion is required and can be grouped into two categories. First, diffusion-dependent transformations involve changes in phase compositions, number of phases, or both, typically producing two phases. An example is the eutectoid reaction in the Fe-C phase diagram shown in Fig. 3.1, where austenite transforms into α-ferrite and cementite below 727°C at 0.76 wt.% carbon. The second category is the diffusionless, or displacive, transformation, in which a metastable phase forms without long-range diffusion, as in martensitic transformation.

Diffusion-dependent transformations require a finite time and their kinetics strongly influence the resulting microstructure. Since phase diagrams do not account for time, isothermal transformation diagrams (or time-temperature-transformation TTT diagrams) are used. These plot temperature versus logarithmic time, with characteristic C-shaped curves indicating the start and finish of transformation.

As shown in Fig. 3.2 the TTT diagram is obtained by first heating the steel into the austenite region until a fully austenitic microstructure is obtained. The material is then cooled rapidly to a chosen temperature and held isothermally. The intersection with the start and finish curves marks the beginning and completion of the transformation, respectively. The upper region of the transformation curve corresponds to the formation of pearlite, a lamellar mixture of α-ferrite and cementite. While lower temperatures produce bainite, consisting of plates or needles of α-ferrite seperated by cementite. Between the curves, transformation is ongoing with a mixture of austenite and the product phase. If cooling is fast enough to avoid intersecting the pearlite or bainite start curves, austenite remains until the martensite start temperature, M_s, is reached, where diffusionless transformation begins. Below M_s, a Body Centered Tetragonal (BCT) α'-martensite forms, with its fraction governed by undercooling rather

than time, explaining the absence of a C-curve for martensite. The different forms of martensite will be further discussed in the following sections.

Martensitic transformation, although athermal and diffusionless, is governed by thermodynamic principles. Its onset is determined by the Gibbs free energy difference between austenite and martensite, which must exceed a critical threshold to overcome transformation barriers. The martensite start temperature M_s corresponds to the point where this driving force becomes sufficient and further cooling increases the transformed fraction. However, the transformation is opposed by stored elastic strain energy and interfacial energies, thereby increasing the driving force required for transformation. Below the martensite finish temperature M_f, any remaining austenite, i.e. retained austenite, remains stable unless additional cooling or applied stress provides the necessary energy for transformation [17–20]. More details on the different energy contributions associated with martensitic transformation, including elastic strain energy and interfacial energy, will be provided in the following section.

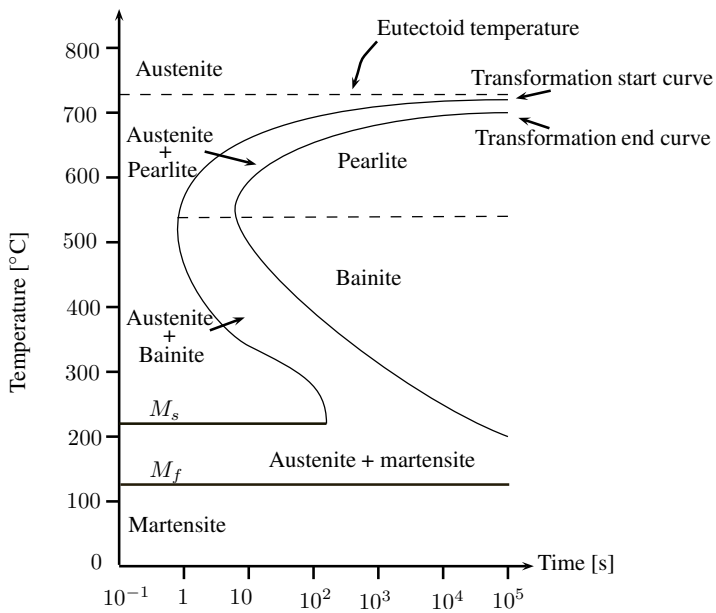

Figure 3.2: Schematic isothermal transformation (TTT) diagram for an Fe-C alloy of eutectoid composition, showing the pearlite, bainite and martensite transformation regions, along with the martensite start temperature, M_s and martensite finish temperature M_f.

3.3 Transformation driving forces and martensite morphology

The transformation from austenite to α'-martensite is governed by the balance of thermodynamic forces and the opposing contributions. Fig. 3.3(a) shows the variation of the chemical free energy of austenite, G_γ, and martensite, $G_{\alpha'}$, as function of temperature. At the temperature T_0, $G_\gamma = G_{\alpha'}$, thus the transformation is expected to occur spontaneously below T_0, however, this is not sufficient in practice. The transformation is opposed by elastic strain energy, arising from lattice distortion required to accommodate martensite within the parent phase, and interfacial energy, associated with the creation of new boundaries between martensite and austenite. Only when the driving force exceeds the sum of these resistance terms the transformation can proceed. At the martensite start temperature M_s, the chemical free energy difference reaches a critical value, $\Delta G^{\gamma\to\alpha'}_{critical}$ sufficient to compensate these energy barriers and initiate transformation. Above M_s, transformation may still occur if the reduction in chemical driving force $\Delta G^{\gamma\to\alpha'}_{chem}$ is compensated by an applied stress, introducing a mechanical contribution $\Delta G^{\gamma\to\alpha'}_{mech}$. Hence a deformation-induced transformation is triggered when the following condition is satisfied

$$\Delta G^{\gamma\to\alpha'}_{chem} + \Delta G^{\gamma\to\alpha'}_{mech} \geq \Delta G^{\gamma\to\alpha'}_{critical} = \Delta G^{\gamma\to\alpha'}_{M_s}. \tag{3.1}$$

Fig. 3.3(b) illustrates the applied stress required to transform austenite to martensite as a function of temperature. Below M_s, transformation occurs spontaneously without applied stress. With increasing temperature, the required stress rises up to M_s^σ, where transformation occurs at pre-existing nucleation sites, referred to as stress-assisted transformation.

For $M_s^\sigma \leq T \leq M_d$, the yield stress of austenite decreases. Austenite initially deforms elastically up to σ_a, followed by plastic deformation, where slip bands and twins form and act as new nucleation sites. Transformation starts at σ_b, defining the strain-induced transformation. The lower stress σ_b compared to the expected σ_c reflects the formation of favorable nucleation sites such as shear band intersections, stacking fault bundles and HCP ε-martensite, which may act as an intermediate or final phase.

At higher temperatures, $M_d \leq T \leq T_0$, the chemical driving force, $\Delta G^{\gamma\to\alpha'}_{chem}$, becomes insufficient and the mechanical contribution $\Delta G^{\gamma\to\alpha'}_{mech}$ cannot compensate, thus only plastic deformation of austenite can be possible, see Fig. 3.3(a), [21–25].

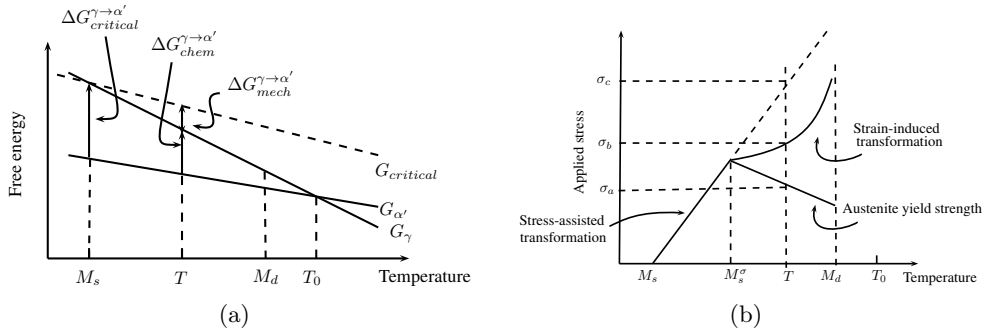

Figure 3.3: (a) Schematic illustration of the thermodynamic driving force for martensitic transformation, showing the free energy of austenite and martensite as a function of temperature together with the chemical and mechanical contributions to the transformation driving force. (b) Schematic representation of the applied stress required to induce martensitic transformation as a function of temperature, illustrating the regimes of spontaneous, stress-assisted and strain-induced transformation.

The displacive transformation when quenching austenite to α'-martensite typically produces a BCT structure which is a distorted BCC lattice, whereas deformation-induced transformation results in martensite with HCP or BCC structures. The Bain model describes this transformation crystallographically, see Fig. 3.4. According to the Bain correspondence, the transformation involves a contraction of approximately 25% along $[001]_\gamma$, which becomes the $[001]_{\alpha'}$, accompanied by an expansion of approximately 13% along $[1\bar{1}0]_\gamma$ and $[110]_\gamma$ which become $[100]_{\alpha'}$ and $[010]_{\alpha'}$, respectively. Carbon atoms, marked as black circles in Fig. 3.4, remain trapped in interstitial sites, causing tetragonal distortion and an increase in unit cell volume. Consequently, the transformation is accompanied by a net volume expansion of the order of 3% with the degree of the tetragonality governed by carbon content [15, 26, 27].

The Bain model provides a crystallographic correspondence between austenite and martensite by describing the FCC to BCT lattice distortions, capturing the essential lattice change. However, it fails to describe the experimentally observed martensitic orientation or the existence of habit planes. The habit plane defines the macroscopic interface between austenite and martensite. Experimentally, this interface is observed to remain approximately undistorted and unrotated during the transformation, providing a compatible boundary between the parent and product phases. To satisfy this condition, the Bain distortion must be combined with a lattice invariant shear, accommodated either by slip or twinning, producing the invariant plane strain. The resulting transformation involves both volume expansion and shear.

This combination does not uniquely determine the martensite orientation

within the austenite, making orientation relationships (ORs) essential. ORs specify the alignment of crystallographic planes and directions between phases, minimizing interfacial misfit and ensuring compatibility. Common examples are the Kurdjumov-Sachs and Nishiyama-Wassermann relationships, which align close-packed planes and directions and link the lattice distortion to the observed martensitic microstructure [8, 15].

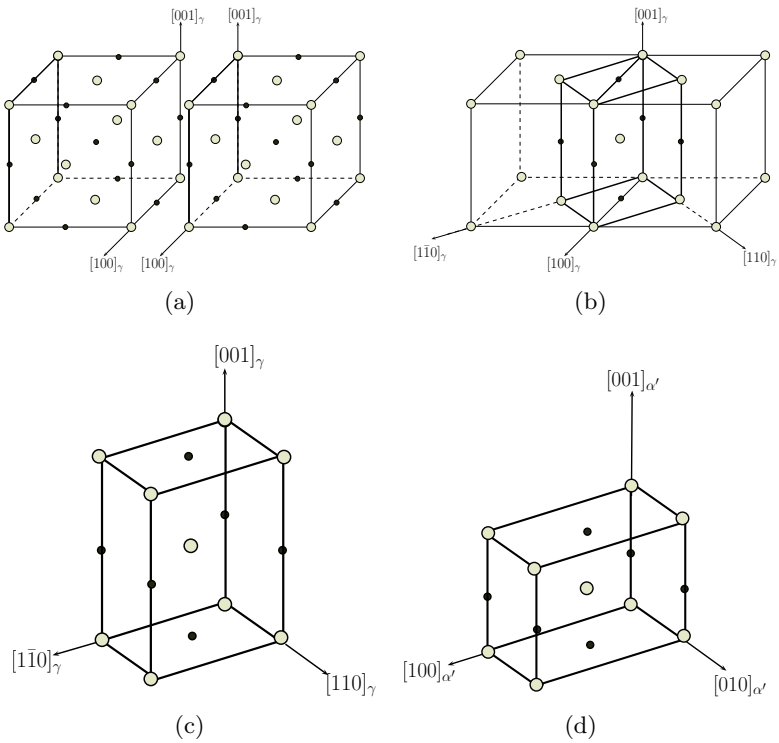

Figure 3.4: Schematic representation of the Bain model for martensitic phase transformation. (a) Two FCC unit cells are shown with intersitial sites marked as black circles. Depending on the carbon content of the steel, a fraction of these sites is randomly occupied by carbon atoms. The cells are joined along their $(010)_\gamma$ planes, giving the configuration in (b) where a BCT unit cell is outlined. For clarity, (b) only includes the iron atoms and the carbon positions of the BCT austenite cell, along with the iron atoms at the corners of the original FCC cells. In (c), the BCT austenite unit cell is shown. Finally the BCT γ-austenite transforms into the BCC/BCT α'-martensite unit cell shown in (d) through a contraction of approximately 25% along $[001]_\gamma$ which becomes the $[001]_{\alpha'}$ and an expansion of approximately 13% along $[1\bar{1}0]_\gamma$ and $[110]_\gamma$ which become $[100]_{\alpha'}$ and $[010]_{\alpha'}$, respectively .

The amount and morphology of martensite are governed by chemical composition, initial grain size and deformation conditions such as temperature, strain rate and stress state. In austenitic steels, alloying elements such as nickel, ni-

trogen, manganese and copper are added to stabilize austenite and improve corrosion resistance and strength. Their concentration influences both the fraction and morphology of martensite. Increasing alloy content suppresses M_s, enhances the austenite stability and suppresses deformation-induced transformation. Carbon content plays a key role, higher amounts promote plate martensite and lower amounts favor lath martensite [22, 28–30].

The parent austenitic grain size influences the transformation as smaller grains increase resistance due to the grain boundaries acting as obstacles to dislocation motion, thereby suppressing martensite formation and promoting deformation twinning.

Deformation at higher temperatures reduces the chemical driving force, see Fig. 3.3(a), thereby decreasing the martensite fraction. At sufficiently high temperatures, strain-induced martensitic transformation is suppressed, resulting in a larger fraction of retained austenite, whose stability is primarily governed by the chemical composition and the deformation temperature.

The strain rate influences the martensite fraction, with higher strain rates promoting α'-martensite formation. The deformation mode is also important as tensile loading generally produces more martensite than compression. Furthermore, the activation of multiple slip systems increases the number of shear-band intersections, thereby enhancing the transformation.

The morphology depends on how lattice invariant shear is accommodated. Slip-dominated shear produces lath martensite, characterized by a high dislocation density and packet structures, which is typically observed in low-carbon steels. A packet consists of parallel laths sharing a common habit plane and is subdivided into blocks of different variants, see Fig. 3.5. In Paper D, the strengthening mechanism of lath martensite, particularly block boundary effects, is modeled. In contrast, twinning-dominated shear leads to plate or needle-like martensite with internal twins, commonly observed in high-carbon steels [1, 8, 15].

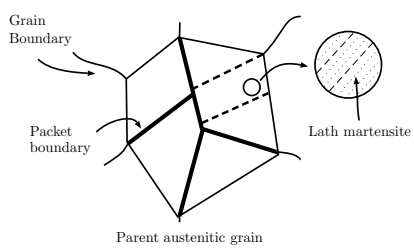

Figure 3.5: Illustration of lath martensite.

3.4 Applications

Martensitic phase transformation is not unique to the iron-carbon system but appears in other ferrous and non ferrous alloy systems. The displacive mechanism is fundamental to numerous engineering and metallurgical applications, including advanced high-strength steels (AHSS), shape memory alloys and surface engineering processes.

Advanced high-strength steels are developed to combine high strength with good ductility and formability, particularly for automotive applications where weight reduction and crash performance are critical. Among the most important classes are the transformation-induced plasticity (TRIP) and dual-phase (DP) steels, whose performance is governed by the presence, morphology and transformation of martensite within the microstructure.

In DP steels, the microstructure consists of a soft ferrite matrix with dispersed islands of martensite. Martensite carries a significant portion of the applied load and induces strain gradients in the surrounding ferrite, leading to high dislocation densities and enhanced work hardening. The interaction between the phases results in a favorable strength-ductility balance. The morphology and distribution of martensite are critical as fine and uniform dispersion improves mechanical performance, whereas coarse or banded martensite can promote strain localization and reduce toughness. This microstructure is typically obtained by intercritical annealing in the $\alpha + \gamma$ region, see Fig. 3.1, followed by rapid cooling to transform austenite into martensite while retaining ferrite [31, 32].

In TRIP steels, martensite forms progressively during deformation through strain-induced transformation of metastable retained austenite. The continuous formation of martensite increases load-bearing capacity and strain hardening, delaying necking and stabilizing plastic flow. Thus, both DP and TRIP steels derive their strength-ductility balance from martensite, either as a pre-existing phase or as a dynamically formed phase during deformation [25, 33, 34].

Another important application of the austenite to martensite transformation is in shape memory alloys (SMAs) where reversible martensitic transformation governs functional behavior. Austenite transforms to martensite upon cooling or applied stress and reverts upon unloading or heating, enabling shape memory and superelasticity. The most common materials that exhibit the shape memory effect are nickel-titanium, copper-based and iron-based alloys. The role of martensite is central, as its formation and reversion provide recoverable strain and actuation capability [2, 35, 36].

Martensitic transformation is also used in surface treatment processes such as shot peening, surface rolling and laser shock peening, where high strain-rate deformation induces transformation of metastable austenite. The result-

ing martensitic surface enhances hardness and introduces compressive residual stresses, improving fatigue and wear resistance [37–42]. The residual state in austenitic steel after laser shock peening has been modeled and studied in Paper A. Similar strain-induced martensitic formation occurs during metal forming processes such as cold rolling and deep drawing, contributing directly to strengthening [24, 43, 44].

In addition, martensitic transformation enhances fracture toughness through transformation toughening. Stress concentrations, such as at crack tips, may induce martensite formation, which absorbs energy and generates compressive stresses, reducing the driving force for crack propagation. This kind of transformation toughening has been observed extensively in TRIP steels and metastable austenitic stainless steels and it is modeled in Paper B [45, 46].

The numerical simulation of the applications discussed in this chapter requires suitable constitutive models. The constitutive frameworks adopted in this thesis are presented in the following chapter.

Chapter 4

Constitutive modeling

Constitutive modeling provides the framework that links materials internal structure to its mechanical response. At the macroscopic level, continuum plasticity models treat the material as a homogeneous continuum, described by yield surfaces, flow rules and hardening laws. Classical models such as Tresca and von Mises form the basis of isotropic plasticity and have been extended to describe plastic flow and hardening behavior. These phenomenological models efficiently reproduce the macroscopic stress-strain response but provide limited insight into the underlying deformation mechanisms [47]. To overcome some of these limitations, constitutive models have been developed that introduce internal variables to represent the evolving material state and formulate the constitutive relations within thermodynamic framework.

Within this framework, internal variable theory is used to represent microstructural evolution through additional state variables, such as backstress and isotropic hardening. These variables capture internal material states that influence macroscopic behavior and enable modeling of cyclic hardening, creep and fatigue [48–50].

Computational modeling of material behavior spans multiple length scales, ranging from atomistic to continuum descriptions, as illustrated in Fig. 4.1. At the smallest length scale, molecular dynamics (MD) simulations explicitly resolve atomic motion by considering interatomic forces and tracking the evolution of individual atoms. This allows studies of dislocation nucleation, defect interactions and transformation interface evolution, and provides parameters such as interface energies and transformation strains. However, MD is limited to small spatial and temporal scales due to its high computational cost.

At a larger length scale, discrete dislocation dynamics (DDD) describes plastic deformation through the collective motion of discrete dislocations. Individual dislocation lines are tracked, including their multiplication, interaction and pile-ups. In the context of martensitic transformation, this approach enables

the modeling of dislocation-assisted nucleation of martensite and the plastic accommodation of transformation-induced strain during martensite growth while allowing larger simulation volumes than MD [51, 52].

At the mesoscale, the crystal plasticity describes deformation at the grain level through slip on crystallographic systems, linking dislocation activity to continuum response and enabling the study of anisotropy, size effects and the microstructural evolution during metal forming processes or phase transformation [53–58]. Other models that operate on the mesoscale are the phase-field methods, which provide a complementary framework for simulating phase transformation and microstructural evolution through a continuous order parameter and diffuse interfaces. By integrating phase-field with other mechanical models, the interaction between deformation, phase boundaries and evolving microstructure can be captured. Phase-field methods are not limited to microstructural evolution but can also be applied into other fields such as topology optimization, fracture mechanics and multiphase fluid dynamics [59–61].

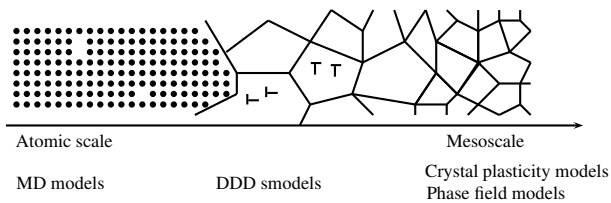

Figure 4.1: Illustration of length scales in modeling.

The choice of modeling approach varies depending on the focus and objectives of the study. In Papers A and B, a continuum model is employed to simulate displacive martensitic phase transformation in austenitic steel under different conditions such as surface treatment and crack propagation, respectively. Continuum modeling is well suited for these processes as they involve large spatial domains and long time scales. In Paper A, the primary interest lies in predicting the phase fraction evolution as well as the residual state and the macroscopic material response after laser shock peening of the material. This can be efficiently captured using homogenized continuum transformation models. Similarly, in Paper B, crack propagation modeling requires stable and computationally efficient description of transformation-induced strain and stress redistribution which makes the continuum approach practical and robust. Papers C and D employ a crystal plasticity framework that incorporate the grain scale. Paper C focuses on the numerical implementation of the crystal plasticity model, whereas Paper D applies the model to analyze the mechanics of lath martensite. The crystal plasticity is well suited for investigating microstructure sensitive phenomena such as deformation behavior at block boundaries in lath

martensite, where slip system interactions strongly influence the mechanical response. Both approaches are thermodynamically consistent formulations that fulfill the first and second laws of thermodynamics.

In the next section, the constitutive frameworks will be presented in a general manner. Fundamental kinematics, together with the first and second laws of thermodynamics, will be introduced. The specific models used in the papers will then be reviewed, followed by a description of the numerical formulations.

4.1 Kinematics and thermodynamics

Constitutive models rely on kinematic quantities that describe how a body $\mathcal{B}$ deforms. A material particle in $\mathcal{B}$ at position $\boldsymbol{X}$ in the reference configuration Ω_0 is mapped to its position at the current configuration Ω as $\boldsymbol{x} = \boldsymbol{\varphi}(\boldsymbol{X}, \boldsymbol{t})$, where t is the time. A line element in the reference configuration $d\boldsymbol{X}$ is related to a line element in the current configuration as $d\boldsymbol{x} = \boldsymbol{F}(\boldsymbol{X}, t)d\boldsymbol{X}$, where $\boldsymbol{F} =$ Grad $\boldsymbol{x}(\boldsymbol{X}, t)$ is the deformation gradient, see Fig. 4.2.

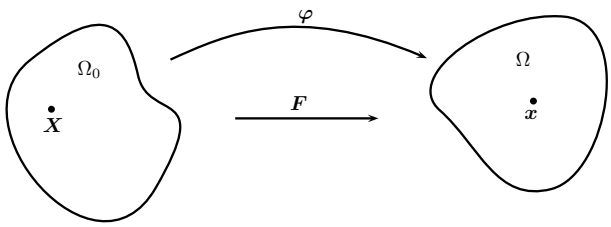

Figure 4.2: Illustration of the deformation of a homogeneous body.

The change in volume between the reference and current configuration at time t is obtained from the determinant of the deformation gradient, $J(\boldsymbol{X}, t) = \det\boldsymbol{F}(\boldsymbol{X}, t) = \rho_0/\rho$, where ρ_0 and ρ are the density in the reference and current configurations respectively. When $J = 1$ at every particle in every configuration and time, it is called isochoric or volume preserving deformation and the volume is kept constant.

Many materials undergo both elastic and inelastic deformation. To describe these mechanisms separately, the total deformation is often decomposed multiplicatively into a reversible part, $\boldsymbol{F}^r$ and an irreversible part $\boldsymbol{F}^{ir}$ as

$$\boldsymbol{F} = \boldsymbol{F}^r \boldsymbol{F}^{ir}. \tag{4.1}$$

The multiplicative decomposition introduces a stress-free intermediate configuration obtained by removing the reversible deformation from the current configuration. The irreversible deformation is described by the mapping from the

reference configuration to the intermediate configuration, whereas the reversible deformation maps the intermediate configuration to the current configuration.

The reversible part of the deformation gradient models elastic deformation, it may also contain other recoverable mechanisms such as thermal deformation. In this thesis, only elastic deformation is considered therefore $\boldsymbol{F}^r = \boldsymbol{F}^e$. The irreversible part, $\boldsymbol{F}^{ir}$, includes the deformation that cannot be recovered. It includes plastic deformation due to slip, $\boldsymbol{F}^p$ and may include deformations due to phase transformation, $\boldsymbol{F}^{tr}$.

The spatial velocity gradient is defined as

$$\boldsymbol{l} = \dot{\boldsymbol{F}}\boldsymbol{F}^{-1}, \tag{4.2}$$

which describes the local rate of motion in the current configuration. Using the multiplicative split of the deformation gradient in (4.1), the spatial velocity gradient can be decomposed as

$$\boldsymbol{l} = \boldsymbol{l}^e + \boldsymbol{l}^{ir} \tag{4.3}$$

where, $\boldsymbol{l}^e = \dot{\boldsymbol{F}}^e\boldsymbol{F}^{e-1}$ and $\boldsymbol{l}^{ir} = \boldsymbol{F}^e\dot{\boldsymbol{F}^{ir}}\boldsymbol{F}^{ir-1}\boldsymbol{F}^{e-1}$.

The constitutive equations governing the material response are formulated within the framework of continuum thermodynamics. The formulation is based on the internal energy u and the entropy S. The first law of thermodynamics expresses the principle of energy conservation. In the current configuration, its local form relates the rate of change of internal energy to the mechanical power, heat generation with strength r per unit mass and the heat flux vector $\boldsymbol{q}$,

$$\rho\dot{u} = \boldsymbol{\sigma} : \mathrm{sym}(\boldsymbol{l}) + \rho r - \mathrm{div}\boldsymbol{q}, \tag{4.4}$$

where $\boldsymbol{\sigma}$ is the Cauchy stress tensor. The notation "sym" denotes the symmetric part of a tensorial quantity and "div" is the spatial divergence operator.

The second law of thermodynamics can be expressed by stating that the entropy production over any thermodynamic cycle cannot be negative. This global statement is formulated mathematically through the Clausius inequality. When the Clausius inequality is localized and combined with the balance of internal energy, it leads to the Clausius-Duhem inequality, which requires that the entropy production at each material point must be non-negative. In local form, this condition can be written as

$$\rho\dot{S} - \frac{\rho r}{\theta} + \frac{1}{\theta}\mathrm{div}\left(\boldsymbol{q}\right) - \frac{1}{\theta^2}\boldsymbol{q}\frac{\partial\theta}{\partial\boldsymbol{x}} \geq 0. \tag{4.5}$$

The Clausius-Duhem inequality is often referred to as the dissipation inequality, which reflects the physical principle that it is impossible to convert heat entirely

into mechanical work, i.e. there must always be a non-negative dissipation $\mathcal{D}$. If the first law (4.4) is inserted into the second law (4.5), then the dissipation inequality can be formulated as:

$$\mathcal{D} = \theta\rho\dot{S} - \rho\dot{u} + \boldsymbol{\sigma} : \mathrm{sym}(\boldsymbol{l}) - \frac{1}{\theta}\boldsymbol{q}\frac{\partial\theta}{\partial\boldsymbol{x}} \geq 0. \tag{4.6}$$

It is standard to reformulate the Clausius-Duhem inequality in a suitable form for constitutive modeling by introducing the Helmholtz free energy, defined as

$$\psi = u - S\theta. \tag{4.7}$$

The Helmholtz free energy is obtained by a Legendre transformation of the internal energy u, which is naturally expressed as a function of the entropy S. The Legendre transformation replaces the entropy as an independent variable by its conjugate variable, namely the absolute temperature θ, so that the Helmholtz free energy is expressed as a function of temperature rather than entropy. It is advantageous to work with ψ instead of u, because the temperature is typically prescribed or measured, whereas entropy is not directly controlled experimentally.

Using the Helmholtz free energy in (4.7) and multiplying the Clausius-Duhem inequality in (4.6) with the determinant of the deformation gradient, J and the absolute temperature, θ, the Clausius-Duhem inequality reads

$$\mathcal{D}_0 = -\rho_0\dot{\psi} + \boldsymbol{\tau} : \mathrm{sym}(\boldsymbol{l}) - \frac{J}{\theta}\boldsymbol{q}\frac{\partial\theta}{\partial\boldsymbol{x}} \geq 0. \tag{4.8}$$

Notice that the dissipation inequality is here formulated in the reference configuration and that $\boldsymbol{\tau} = J\boldsymbol{\sigma}$ is the Kirchhoff stress tensor. In this thesis, only isothermal conditions are considered, thus the last term in the dissipation is equal to zero.

The Helmholtz free energy is formulated as a function of a set of state variables, $\boldsymbol{A}$, including the temperature together with variables describing the reversible and irreversible material response. The dissipation inequality can then be written as

$$\mathcal{D}_0 = \boldsymbol{\tau} : \mathrm{sym}(\boldsymbol{l}) - \rho_0\frac{\partial\psi}{\partial\boldsymbol{A}} : \dot{\boldsymbol{A}} \geq 0. \tag{4.9}$$

In finite strain plasticity, the state variables typically consist of the elastic deformation via the elastic right Cauchy-Green tensor $\boldsymbol{C}^e = \boldsymbol{F}^{eT}\boldsymbol{F}^e$, or the elastic left Cauchy-Green tensor $\boldsymbol{b}^e = \boldsymbol{F}^e\boldsymbol{F}^{eT}$. The state is further characterized by a set of internal, or state, variables α_i which describes the irreversible response of the material, including quantities such as the plastic deformation gradient, hardening variables or transformation variables associated with martensitic phase

transformation. If the elastic deformation gradient $\boldsymbol{F}^e$ is used, the dissipation inequality reads

$$\mathcal{D}_0 = \boldsymbol{\tau} : \mathrm{sym}(\boldsymbol{l}^e) + \boldsymbol{\tau} : \mathrm{sym}(\boldsymbol{l}^{ir}) - \rho_0 \frac{\partial \psi}{\partial \boldsymbol{F}^e} \dot{\boldsymbol{F}}^e - \rho_0 \sum_i \frac{\partial \psi}{\partial \alpha_i} \dot{\alpha}_i \geq 0. \tag{4.10}$$

Since the elastic processes are reversible, thus the elastic contribution must vanish for all admissible elastic strain rates. Enforcing this condition leads to

$$\mathcal{D}_0^e = \boldsymbol{\tau} : \mathrm{sym}(\boldsymbol{l}^e) - \rho_0 \frac{\partial \psi}{\partial \boldsymbol{F}^e} \dot{\boldsymbol{F}}^e = 0, \tag{4.11}$$

which allows the stress to be identified as

$$\boldsymbol{\tau} = 2\rho_0 \frac{\partial \psi}{\partial \boldsymbol{F}^e} \boldsymbol{F}^e. \tag{4.12}$$

Inserting (4.12) into (4.10) yields

$$\mathcal{D}_0^{ir} = \boldsymbol{\tau} : \mathrm{sym}(\boldsymbol{l}^{ir}) + \rho_0 \sum_i Y_i \dot{\alpha}_i > 0 \tag{4.13}$$

where $Y_i = -\frac{\partial \psi}{\partial \alpha_i}$ are the conjugate thermodynamic forces that drive the state variables α_i.

The dissipation inequality alone does not uniquely determine the evolution of the irreversible processes. Additional constitutive assumptions are therefore required to define the evolution of the irreversible deformation and the internal variables. A common approach is to introduce a convex potential, g, from which the evolution equations are obtained as

$$\mathrm{sym}(\boldsymbol{l}^{ir}) = \lambda \frac{\partial g}{\partial \boldsymbol{\tau}}, \tag{4.14}$$

$$\dot{\alpha}_i = \lambda \frac{\partial g}{\partial Y_i}. \tag{4.15}$$

where λ is a non-negative multiplier. The evolution equations determine the direction of the irreversible evolution. Whether irreversible evolution occurs is determined by an admissible domain defined by a function f, which may correspond, for example, to the yield function in plasticity. States satisfying $f < 0$ lie inside the admissible domain, where the material response is purely reversible and the evolution of the state variables vanishes, $\dot{\alpha}_i = 0$. The boundary $f = 0$ represents the onset of irreversible evolution. When the state reaches this boundary and further loading tends to violate the admissibility condition, the evolution is activated through the multiplier λ, and the Kuhn-Tucker conditions,

$$\lambda \geq 0, \quad f \leq 0, \quad \lambda f = 0, \tag{4.16}$$

ensure the admissibility of the material response. The material state remains inside or on the boundary of the admissible domain and the evolution never goes backward. Moreover, the consistency condition $\dot{f} = 0$ for $\lambda > 0$ determines λ.

Different choices of the convex potential, g, lead to different constitutive models. In an associated model, the evolution law is obtained from a potential that is identical to the function f, i.e. $g = f$. The evolution rate equations take the form

$$\mathrm{sym}(\boldsymbol{l}^{ir}) = \lambda \frac{\partial f}{\partial \boldsymbol{\tau}}, \tag{4.17}$$

$$\dot{\alpha}_i = \lambda \frac{\partial f}{\partial Y_i}. \tag{4.18}$$

In an associated model, the flow direction $\frac{\partial f}{\partial Y_i}$ is normal to the boundary $f = 0$ and the dissipation is maximized among all admissible directions as well as a the evolution is thermodynamically efficient. On the contrary, in a non-associated approach, the direction of the evolution of the internal variables is obtained from the convex potential g that is independent of the function defining the admissible state. It can be formulated as in (4.14) and (4.15). This allows the evolution direction to differ from the normal to the admissible boundary while still requiring that $Y_i \dot{\alpha}_i \geq 0$ [47, 62].

In the following sections, the continuum model employed in Papers A and B to simulate the martensitic phase transformation is presented, followed by the crystal plasticity model used in Papers C and D.

4.2 Continuum mechanical model

To simulate the displacive martensitic phase transformation in steels, a continuum model at the macroscopic scale is used in Paper A and B. The model is thermodynamically consistent and is originally established in [63, 64]. In the model, the irreversible mechanical state includes plastic deformations due to slip and plastic deformations due to phase transformation, thus the two processes plasticity and phase transformation may occur independently of each other and are described through a plastic yield surface and a transformation potential. The set of internal variables in the model consist of $\boldsymbol{A} = \{\boldsymbol{b}^e, \kappa_i, z, \theta\}$, where κ_i are the isotropic hardening parameters, $z \in [0, 1]$ the volume fraction of martensite and θ is the absolute temperature, here being a parameter since isothermal conditions are considered. The volume fraction of martensite being zero, $z = 0$, indicates that only austenite is present, while $z = 1$ indicates that only martensite is present. The hardening parameters account for both hardening due to plastic slip, i.e. increased dislocation density, and hardening associated with the evolution of the martensitic phase.

To define the evolution of plasticity and phase transition, the spatial velocity gradient $\boldsymbol{l}^{ir}$ is split into a plastic and transformation part:

$$\boldsymbol{l}^{ir} = \boldsymbol{l}^{p} + \boldsymbol{l}^{tr}. \tag{4.19}$$

Using (4.19) and the thermodynamic forces

$$\rho_0 \frac{\partial \psi}{\partial \kappa_i} = R_i, \quad \rho_0 \frac{\partial \psi}{\partial z} = Q, \tag{4.20}$$

the dissipation inequality in (4.13) can be subdivided into plastic, $\mathcal{D}_0^p$, and transformational, $\mathcal{D}_0^{tr}$, parts according to

$$\mathcal{D}_0^p = \boldsymbol{\tau} : \mathrm{sym}(\boldsymbol{l}^p) - \sum_i R_i \dot{\kappa_i} \geq 0, \quad \mathcal{D}_0^{tr} = \boldsymbol{\tau} : \mathrm{sym}(\boldsymbol{l}^{tr}) - Q\dot{z} \geq 0, \tag{4.21}$$

In (4.21), the Kirchhoff stress tensor is defined using the elastic left Cauchy-Green tensor $\boldsymbol{b}^e$ as

$$\boldsymbol{\tau} = 2\rho_0 \frac{\partial \psi}{\partial \boldsymbol{b}^e} \boldsymbol{b}^e. \tag{4.22}$$

Since the temperature θ is considered a parameter, thus $\frac{\partial \psi}{\partial \theta} = 0$ and the dissipation does not include a thermal part.

Defining admissible domain for plasticity, $\mathcal{P}(z, \theta)$, and an admissible domain for phase transformation, $\mathcal{T}(\theta)$, allows a purely elastic domain to be defined as

$$\mathcal{E} = \mathcal{P} \cap \mathcal{T}. \tag{4.23}$$

This is in accordance with the understanding of stress-assisted transformation where phase transition can take place within $\mathcal{P}$ also when no plastic strains develop. The model can also capture a plastic response when no transformation strains are developed.

Defining admissible domains for plasticity and phase transformation establishes the conditions under which the different irreversible mechanisms become active. The constitutive framework presented so far is rate-independent. For the laser shock peening application considered in Paper A, the material experiences very high strain rates, requiring the constitutive model to account for rate-dependent effects. Whereas plasticity primarily is governed by the motion of dislocations, the martensitic phase transformation is assumed to occur instantaneously. It is therefore assumed that rate dependency affects only the plastic response. Furthermore, it is assumed that the rate dependency influences only the yield surface and not the hardening. In Paper A, a dynamic yield surface based on the Cowper-Symonds relation is utilized,

$$\sigma_{y0}^d = \sigma_{y0} \left[1 + \left(\frac{\dot{\epsilon}_{eff}^p}{\dot{\epsilon}_0} \right)^{1/p} \right], \tag{4.24}$$

where $\dot{\epsilon}^p_{eff}$ is the effective plastic strain, $\dot{\epsilon}_0$ is a reference strain rate and p is a parameter that controls the strain rate sensitivity.

The specific model and the choice of the Helmholtz free energy as well as the evolution laws for the internal variables are further shown in Paper A and B.

4.3 Crystal plasticity model

In crystal plasticity based models, the total deformation is also decomposed into an elastic and a plastic part as in (4.1). Following [65], the set of internal variables in the model consist of $\boldsymbol{A} = \{\boldsymbol{C}^e_i, J, g^\alpha\}$, where $\boldsymbol{C}^e_i$ is the isochoric part of the elastic right Cauchy Green tensor and g^α represents the slip resistance of slip system α. In contrast to the continuum formulation, plastic deformation is described by crystallographic slip on the individual slip systems. Consequently, the constitutive response is governed by the evolution of the slip rates, $\dot{\gamma}^\alpha$, together with the hardening variables g^α. The superscript α, which ranges from 1 to n, denotes the slip system, where n is the total number of slip systems present in a crystal. The Helmholtz free energy is split into an elastic and a plastic part as

$$\rho_0\psi(\boldsymbol{C}^e_i, J, g^\alpha) = \rho_0\psi^e(\boldsymbol{C}^e_i, J) + \rho_0\psi^p(g^\alpha). \tag{4.25}$$

As $\boldsymbol{C}^e_i$ and J are both functions of elastic deformation tensor, $\boldsymbol{C}^e$, thus the dissipation inequality takes the form

$$\mathcal{D}_0 = \boldsymbol{\tau} : \mathrm{sym}(\boldsymbol{l}^e) + \boldsymbol{\tau} : \mathrm{sym}(\boldsymbol{l}^p) - \rho_0 \frac{\partial \psi^e}{\partial \boldsymbol{C}^e}\dot{\boldsymbol{C}}^e - \rho_0 \sum_\alpha \frac{\partial \psi^p}{\partial g^\alpha} \geq 0, \tag{4.26}$$

As the elastic contribution vanishes for all admissible elastic strain rates, thus the Kirchhoff stress tensor can be identified as:

$$\boldsymbol{\tau} = 2\rho_0 \boldsymbol{F}^e \frac{\partial \psi^e}{\partial \boldsymbol{C}^e}(\boldsymbol{F}^e)^T. \tag{4.27}$$

Using the Kirchhoff stress tensor in (4.27), the plastic part of the dissipation inequality can be expressed as the following:

$$\mathcal{D}^p_0 = \boldsymbol{\Sigma} : \boldsymbol{L}^p - \sum_\alpha G^\alpha \dot{g}^\alpha \tag{4.28}$$

where $\Sigma = 2\rho_0 \boldsymbol{C}^e \frac{\partial \psi}{\partial \boldsymbol{C}^e}$ is the Mandel stress tensor, $G^\alpha = \rho_0 \frac{\partial \psi}{\partial g^\alpha}$ are the thermodynamic forces associated with the hardening and $\boldsymbol{L}^p = \dot{\boldsymbol{F}}^p \boldsymbol{F}^{p-1}$ is the plastic velocity gradient.

The plastic velocity gradient is expressed as the sum of the slip rates on all slip systems,

$$\boldsymbol{L}^p = \sum_{\alpha=1}^{n} \dot{\gamma}^\alpha \boldsymbol{M}^\alpha \otimes \boldsymbol{N}^\alpha. \tag{4.29}$$

Here, $\boldsymbol{M}^\alpha$ and $\boldsymbol{N}^\alpha$ denote the slip direction and the normal to the slip plane of slip system α, respectively. The plastic velocity gradient is defined in the intermediate configuration since it is associated with the plastic deformation gradient $\mathbf{F}^p$. Consequently, the slip directions and slip plane normals are also defined in the intermediate configuration. The orientation of the slip systems is assumed to remain unchanged during the elastic deformation, i.e. the intermediate configuration is assumed to be isoclinic.

The remaining constitutive assumption is therefore the evolution law governing the slip rates, $\dot{\gamma}^\alpha$. It may be formulated in either a rate-independent or a rate-dependent manner. In the present work, a rate-dependent formulation is adopted. Rate-dependent models are capable of capturing viscoplastic phenomena such as creep, whereas rate-independent formulations neglect strain rate effects and assume that plastic deformation occurs instantaneously once the resolved shear stress on a slip system exceeds a critical threshold. This idealization can introduce numerical challenges, particularly in the determination of active slip systems, where the solution may be non-unique leading to increased computational complexity. In a rate-dependent formulation, the slip rate is expressed as a continuous function of the resolved shear stress. Consequently, all slip systems are considered to be potentially active at all times, although slip on systems with stresses well below the slip resistance remain negligible. This eliminates the need to determine the active slip systems explicitly. The resulting constitutive equations form a system of stiff differential equations. Following [65], the slip rate on each slip system is described by the power-law type flow rule as

$$\dot{\gamma}^\alpha = \dot{\gamma}_0 \left(\frac{\tau^\alpha}{G_0 + G^\alpha} \right)^m \operatorname{sgn}(\tau^\alpha). \tag{4.30}$$

In (4.30), $\dot{\gamma}_0$ is the reference slip rate, τ^α is the resolved shear stress and the exponent m is a sensitivity parameter. The slip rate therefore increases continuously with the resolved shear stress relative to the slip resistance. The resolved shear stress is defined in terms of the projection of the Mandel stress tensor $\boldsymbol{\Sigma}$ onto the different slip systems as

$$\tau^\alpha = \boldsymbol{M}^\alpha \boldsymbol{\Sigma} \boldsymbol{N}^\alpha. \tag{4.31}$$

For higher values of m, a rate-independent response is approached. The slip resistance $(G_0 + G^\alpha)$ is composed of a constant term G_0 and a slip system

specific term G^α which depends on the internal hardening variable g^α. The choice of the Helmholtz free energy is further shown in Paper C and D.

In Paper D, the crystal plasticity model is used to simulate the behavior of lath martensite. A strengthening mechanism similar to grain refinement is observed in lath martensite, The block boundaries within lath martensite serve as internal barriers to dislocation motion, thereby contributing to the overall hardening of the material. The influence of these block boundaries is modeled using a Hall-Petch type relationship, capturing their contribution to the material strength. The slip resistance G_0 in (4.30) is modeled to depend on the distance to the block boundaries as

$$G_0(d) = \hat{G}_0 \left(1 + \frac{k}{\sqrt{d}}\right) \tag{4.32}$$

where the parameters $\hat{G}_0$ and k control the influence of the block size strengthening and d is the distance to the block boundary. The Hall-Petch parameter k needs to be identified for each specific alloy that is being studied, see Paper D.

Chapter 5

Numerical implementation

The constitutive equations derived in the previous chapter must be integrated within a boundary value problem governed by the balance laws of continuum mechanics. In the finite element framework, this leads to a problem with two interacting levels. At the global level, the balance of linear momentum governs the deformation of the body, whilst the constitutive equations describe the local stress response and the evolution of the microstructural variables at the integration points. In the next sections, the governing equilibrium equation is presented alongside numerical procedures employed to solve the resulting non-linear boundary value problem and the associated constitutive equations.

5.1 Balance equations

The balance of linear momentum constitutes the governing equation of the mechanical problem. Together with the prescribed boundary conditions, it defines the strong form of the boundary value problem. Under quasi-static conditions, where inertial effects are neglected, the local form of the balance equation in the current configuration is given by

$$\mathrm{div}\boldsymbol{\sigma} + \boldsymbol{b} = \boldsymbol{0}, \tag{5.1}$$

where $\boldsymbol{b}$ is body force per unit current volume. The strong form is reformulated into its corresponding weak form by applying the principle of virtual work and is subsequently discretized using the finite element method.

5.2 Numerical procedure

Following the weak formulation and finite element discretization of the boundary value problem, the coupled equilibrium and constitutive equations take the form

$$\begin{aligned} \mathcal{R}(\boldsymbol{a}, \boldsymbol{z}, t) &= \boldsymbol{0} \\ \dot{\boldsymbol{z}} &= \boldsymbol{f}(\boldsymbol{z}, t) \end{aligned} \tag{5.2}$$

where $\mathcal{R}(\boldsymbol{a}, \boldsymbol{z}, t)$ denotes the nonlinear residual vector associated with the finite element discretization of the equilibrium equation. It depends on the nodal displacement vector, $\boldsymbol{a}$, the vector of internal variables at the integration points, $\boldsymbol{z} = \begin{bmatrix} \boldsymbol{\alpha}_i & \boldsymbol{F}^{ir} \end{bmatrix}^T$, and the time, t. The equation (5.2)(b), represents the constitutive evolution equations governing the internal variables, while the explicit time dependence originates from the prescribed loading and boundary conditions.

The coupled system in (5.2) consists of two fundamentally different classes of equations. The equilibrium equation, represented by the residual vector $\mathcal{R}$, forms a nonlinear algebraic system arising from the finite element discretization of the balance of linear momentum. In contrast, the constitutive equations are expressed as a system of first-order ordinary differential equations describing the evolution of the internal variables. Consequently, different numerical procedures are required for their solution. The equilibrium equations are solved globally using Newton-Raphson iterations, whereas the constitutive evolution equations are integrated locally at each integration point [47].

At each integration point, the constitutive evolution equations define an initial value problem that requires numerical time integration. The time interval $t \in [t_0, t_N]$ is divided into n increments of size Δt_n and the solution at the end of each increment is approximated by $\boldsymbol{z}(t_{n+1}) \approx \boldsymbol{z}_{n+1}$. The choice of the time integration scheme determines how the differential equations are transformed into algebraic equations that can be solved numerically.

Explicit time integration schemes evaluate the evolution function using only known quantities at the beginning of the current time step. These methods are straightforward to implement and are computationally inexpensive since no nonlinear system has to be solved during the constitutive update. A simple example is the forward Euler method,

$$\boldsymbol{z}_{n+1} = \boldsymbol{z}_n + \Delta t_n \boldsymbol{f}(\boldsymbol{z}_n, t_n). \tag{5.3}$$

Since the right-hand side contains only known quantities, the updated internal variables are obtained directly. Explicit methods are, however, only conditionally stable and therefore require sufficiently small time increments. They are primarily employed in dynamic simulations, where the global equilibrium equations are also integrated explicitly and small time increments are already dictated by the stability requirements of the dynamic analysis.

Implicit integration schemes evaluate the evolution equations at the unknown state of the current increment. The backward Euler method, for example, is written as

$$\boldsymbol{z}_{n+1} = \boldsymbol{z}_n + \Delta t_n \boldsymbol{f}(\boldsymbol{z}_{n+1}, t_{n+1}). \tag{5.4}$$

Unlike the explicit formulation, the unknown internal variables appear implicitly on both sides of the equation. Consequently, the time discretization converts the differential equation into a nonlinear algebraic system, which is typically solved using Newton-Raphson iterations at each integration point. Although implicit methods require the solution of a nonlinear system at every time increment, they provide improved stability properties and permit substantially larger time increments, making them particularly suitable for stiff constitutive models and quasi-static simulations.

Many constitutive models are implemented within an elastic predictor-plastic corrector structure. In this approach, the material response is first evaluated assuming purely elastic behavior. The admissibility conditions are then verified and, if violated, a correction step is performed to update the plastic variables and restore consistency with the constitutive equations. This predictor-corrector strategy is commonly combined with implicit integration schemes because of their robustness and numerical stability when integrating highly nonlinear constitutive equations.

The Runge-Kutta family represents another important class of time integration methods. Instead of evaluating the evolution equations only once during a time increment, Runge-Kutta methods compute a sequence of intermediate stage values allowing higher-order accuracy to be achieved. These intermediate stages can be evaluated either explicitly or implicitly, depending on the specific formulation. The general Runge-Kutta approximation of (5.2)(b) is given by

$$\boldsymbol{z}_{n+1} = \boldsymbol{z}_n + \Delta t_n \sum_{i=1}^{s} b_i k_i, \tag{5.5}$$

where s is the number of stages in the Runge-Kutta scheme, b_i are weight parameters and k_i are the stage derivatives. In the case of explicit Runge-Kutta scheme, the stage derivatives are given as

$$k_i = \boldsymbol{f}\left(\boldsymbol{z}_n + \Delta t_n \sum_{j=1}^{i-1} a_{ij} k_j, t_n + c_i \Delta t_n\right), \tag{5.6}$$

where c_i are the coefficients that denotes the stage nodes. It can be seen that each stage depends only on previously computed stages. Consequently the stage values are evaluated sequentially without requiring the solution of nonlinear

equations. For implicit Runge-Kutta methods, the state derivatives k_i are evaluated as

$$k_i = \boldsymbol{f}\left(\boldsymbol{z}_n + \Delta t_n \sum_{j=1}^{s} a_{ij} k_j, t_n + c_i \Delta t_n\right), \tag{5.7}$$

so that the stage equations become coupled and depend on unknown stage values. As a result, a nonlinear system must be solved, typically using Newton-Raphson iterations. Although this increases the computational cost, implicit Runge-Kutta methods possess excellent stability properties and can achieve high orders of accuracy while remaining suitable for stiff problems.

A particularly attractive subclass is the diagonally implicit Runge-Kutta (DIRK) methods, for which the Runge-Kutta coefficient matrix is lower triangular with non-zero diagonal entries. Consequently, the stage equations are solved sequentially rather than simultaneously, reducing the computational effort compared with fully implicit Runge-Kutta methods while largely preserving their favorable stability properties.

In paper C, a two-stage DIRK algorithm is used to solve the crystal plasticity constitutive equations. Crystal plasticity simulations generally involve a large number of grains with different crystallographic orientations, resulting in a substantial number of constitutive updates at each time increment. Furthermore, the rate-dependent power-law slip formulation, cf. (4.30), becomes increasingly stiff for small values of the rate sensitivity parameter, m, requiring robust integration algorithms. The DIRK method provides higher-order temporal accuracy than the backward Euler method while maintaining excellent stability for stiff constitutive equations. Within the proposed formulation, the coupled equilibrium and constitutive equations are treated as a system of differential-algebraic equations (DAEs), in which the equilibrium equations constitute the algebraic constraints and the constitutive equations provide the differential part. The resulting nonlinear stage equations are solved using Newton-Raphson iterations. The complete formulation and algorithmic implementation are presented in Paper C, where the DIRK approach is shown to provide significantly higher accuracy than the conventional backward Euler integration used for comparison.

Finally, several alternative integration strategies have been proposed in the literature. Semi-implicit methods combine explicit and implicit discretizations by treating only selected parts of the constitutive equations implicitly, thereby reducing the computational cost while retaining improved stability compared with purely explicit methods. Operator-splitting and staggered solution procedures decouple different groups of unknowns and solve them sequentially within a single time increment. Considering the system in (5.2), the residual equation may be solved first while keeping the internal variables fixed, followed by a separate update of the constitutive evolution equations. Such approaches may

simplify the numerical implementation and reduce the computational effort, although additional iterations are often required to recover consistency between the coupled fields. The selection of a suitable integration strategy ultimately depends on the characteristics of the constitutive model, the required accuracy, the computational efficiency and the degree of stiffness of the governing evolution equations [47, 66–70].

Chapter 6

List of appended papers

This doctoral thesis is based on the following papers:

Paper A

M. Halilovič, S. Issa, M. Wallin, H. Hallberg, M. Ristinmaa (2016)
Prediction of the residual state in 304 austenitic steel after laser shock peening - effects of plastic deformation and martensitic phase transformation. International Journal of Mechanical Sciences, volume 111-112, pages 24-34.

Paper B

S. Issa, S. Eliasson, A. Lundberg, M. Wallin, H. Hallberg (2018)
Cohesive zone modeling of crack propagation influenced by martensitic phase transformation. Materials Science and Engineering: A (2018), volume 712, pages 564-573.

Paper C

S. Issa, M. Wallin, M. Ristinmaa, H. Hallberg (2018)
Diagonally Implicit Runge-Kutta (DIRK) integration applied to finite strain crystal plasticity modeling. Computational Mechanics (2018), volume 62, pages 1429-1441.

Paper D

S. Issa, H. Hallberg, M. Wallin, M. Ristinmaa (2025)
Efficient Crystal Plasticity Modeling of Lath Martensite Considering Block Boundary Effects. Metals (2025), volume 15(4), 435.

6.1 Own contribution

The overall research direction, formulation of objectives and interpretation of the results in the appended papers were carried out in close collaboration with the co-authors.

In Paper A, the model development and analysis were conducted in collaboration with the first author, who was responsible for the numerical implementation. The author of this thesis contributed to the formulation and evaluation of the model and took the main responsibility for preparing and writing the paper.

In Paper B, the model development, analysis and numerical implementation were carried out in collaboration with the co-authors. The author of this thesis took the main responsibility for preparing and writing the paper.

In Papers C and D, the model development, analysis and numerical implementation were carried out by the author of this thesis. The analysis and interpretation of the results were conducted in collaboration with the co-authors. The author of this thesis also took the main responsibility for preparing and writing the papers.

6.2 Summary of appended papers

Paper A: In Paper A, an elasto-plastic continuum model that includes martensitic phase transformation is extended to capture the rate dependency of plastic deformation during Laser Shock Peening (LSP). The influence of temperature, laser pulse duration and laser intensity on the residual state after LSP is studied. It is shown that both phase transformation and plasticity are important mechanisms during LSP and that both generate residual stresses.

Paper B: In Paper B, a continuum model is used together with a cohesive zone model to investigate the influence of martensitic phase transformation on crack propagation. The continuum model considers austenite to martensite phase transformation coupled to large strain plasticity and different martensite dependent cohesive models are investigated. As martensitic phase transformation is strongly temperature dependent, thus different isothermal settings are considered. It is verified that at lower temperatures, martensitic phase transformation retards crack propagation to a greater extent.

Paper C: In Paper C, the Diagonally Implicit Runge-Kutta method (DIRK) is evaluated and compared to solution procedures for finite element strain crystal plasticity boundary value problems. The structure of the DIRK implementation is similar to that of a conventional implicit backward Euler scheme. It is shown

that only very small modifications are required in order to transform the numerical scheme from one into the other. It is shown that the two-stage DIRK scheme combined with a step size control and a time continuous projection technique for the update of the plastic deformation gradient is in general more accurate than the implicit backward Euler.

Paper D: In Paper D, the influence of block boundaries in lath martensite is studied. A compact and efficient rate-dependent crystal plasticity model that incorporates block boundary effects in lath martensite is used. The block boundary effects are incorporated by a Hall-Petch-type block size dependence and it is shown that the model provides simulation results which agree well with findings from experimental studies where block boundaries contribute to the macroscopic strength of the material.

Chapter 7

Future Perspectives

In this thesis, two complementary modeling approaches are employed: a continuum-scale constitutive model describing the martensitic phase transformation in austenitic steel and a crystal plasticity framework used to simulate the mechanical behavior of both austenitic and martensitic steels at the level of individual crystals and slip systems.

Future work may focus on further integrating these two approaches by extending the crystal plasticity model to account for phase transformation at the crystal level. Crystal plasticity frameworks incorporating deformation-induced martensitic transformation have been proposed in recent years [71, 72]. Extending the framework developed in this thesis to account for transformation kinetics within individual grains based on the local stress state, accumulated plastic deformation or thermodynamic driving forces, would enable the interaction between crystallographic slip and martensitic transformation to be described at the grain level.

In addition, machine learning and data-driven techniques offer promising tools for improving model calibration and predictive capability. They can be used for parameter identification and inverse calibration of crystal plasticity models using experimental data, reducing the computational cost compared to conventional optimization procedures [73, 74]. Combined with physics-based constitutive models, these techniques may improve the efficiency and robustness of parameter calibration while preserving the underlying physical interpretation of the constitutive framework.

Bibliography

[1] W. D. Callister, D. G. Rethwisch, Materials Science and Engineering: An Introduction, John Wiley & Sons, Hoboken, New Jersey, 2018.

[2] H. Stroud, D. Hartl, Shape memory alloy torsional actuators: a review of applications, experimental investigations, modeling, and design, Smart Materials and Structures 29 (11).

[3] L. Pun, V. Langi, A. R. Ruiz, M. Isakov, M. Hokka, In-situ synchrotron x-ray diffraction study of the effects of grain orientation on the martensitic phase transformations during tensile loading at different strain rates in metastable austenitic stainless steel, Materials Science and Engineering: A 900 (2024) 146481.

[4] F. Niessen, A. A. Gazder, J. Hald, M. A. Somers, Multiscale in-situ studies of strain-induced martensite formation in inter-critically annealed extra-low-carbon martensitic stainless steel, Acta Materialia 220 (2021) 117339.

[5] Y. Onuki, S. Sato, In situ observation for deformation-induced martensite transformation during tensile deformation of sus 304 stainless steel by using neutron diffraction part ii: Transformation and texture formation mechanisms, Quantum Beam Science 5 (1) (2021) 6.

[6] F. Niessen, E. Pereloma, A review of in situ observations of deformation-induced $\beta \leftrightarrow \alpha'$ martensite transformations in metastable β ti alloys, Advanced Engineering Materials 24 (7) (2022) 2200281.

[7] W. L. Bragg, J. F. Nye, A dynamical model of a crystal structure, Proceedings of the Royal Society of London. Series A. Mathematical and Physical Sciences 190 (1023) (1947) 474–481.

[8] R. E. Smallman, R. J. Bishop, Modern Physical Metallurgy and Materials Engineering, Butterworth-Heinemann, 1999.

[9] D. Hull, D. Bacon, Introduction to Dislocation, 5th Edition, Elsevier Ltd, 2011.

[10] P. Thome, M. Schneider, V. A. Yardley, E. J. Payton, G. Eggeler, Local maxima in martensite start temperatures in the transition region between lath and plate martensite in fe-ni alloys, Materials 16 (4) (2023) 1549.

[11] H. K. D. H. Bhadeshia, Geometry of Crystals, Polycrystals, and Phase Transformations, Taylor and Francis Group, 2018.

[12] H. Bunge, Texture Analysis in Materials Science: Mathematical Methods., Butterworth and Co, 1982.

[13] R. B. Figueiredo, M. Kawasaki, T. G. Langdon, Seventy years of hall-petch, ninety years of superplasticity and a generalized approach to the effect of grain size on flow stress, Progress in Materials Science 137 (2023) 101131.

[14] S. Xu, Y. Zhao, D. Chen, L. Sun, L. Chen, X. Tong, C. Liu, Z. Zhang, Nanoscale precipitation and its influence on strengthening mechanisms in an ultra-high strength low-carbon steel, International Journal of Plasticity 113 (2019) 99–110.

[15] H. Bhadeshia, Theory of Transformations in Steels, CRC Press, 2021.

[16] E. Pereloma, D. V. Edmonds (Eds.), Phase Transformations in Steels., Vol. 2, Woodhead Publishings, 2012.

[17] R. Salzbrenner, M. Cohen, On the thermodynamics of thermoelastic martensitic transformations, Acta Metallurgica 27 (5) (1979) 739–748.

[18] H. K. D. H. Bhadeshia, Driving force for martensitic transformation in steels, Metal Science 15 (4) (1981) 175–177.

[19] M. Frichtl, S. Ankem, Computational-thermodynamics-based martensite-start temperature models, Calphad 88 (2025) 102776.

[20] S. Mirhosseini, E. Perdahcioglu, E. Atzema, A. van den Boogaard, Effect of temperature and heat generation on martensitic phase transformation in dh steels, Results in Materials 14 (2022) 100281.

[21] G. Olson, M. Cohen, A mechanism for the strain-induced nucleation of martensitic transformations, Journal of the Less Common Metals 28 (1) (1972) 107–118.

[22] P. C. Maxwell, A. Goldberg, J. C. Shyne, Stress-assisted and strain-induced martensites in fe-ni-c alloys, Metallurgical Transactions 5 (6) (1974) 1305–1318.

[23] P. L. Mangonon, G. Thomas, The martensite phases in 304 stainless steel, Metallurgical Transactions 1 (6) (1970) 1577–1586.

[24] M. J. Sohrabi, M. Naghizadeh, H. Mirzadeh, Deformation-induced martensite in austenitic stainless steels: A review, Archives of Civil and Mechanical Engineering 20 (4) (2020) 124.

[25] A. Jain, A. Varshney, A critical review on deformation-induced transformation kinetics of austenitic stainless steels, Materials Science and Technology 40 (2) (2024) 75–106.

[26] E. C. Bain, The nature of martensite, The American Institute of Mining, Metallurgical, and Petroleum Engineers, 1924.

[27] H. Bhadeshia, R. Honeycombe, Chapter 5 - formation of martensite, in: Steels: Microstructure and Properties (Fourth Edition), Butterworth-Heinemann, 2017, pp. 135–177.

[28] L. E. Murr, K. P. Staudhammer, S. S. Hecker, Effects of Strain State and Strain Rate on Deformation-Induced Transformation in 304 Stainless Steel: Part II. Microstructural Study, Metallurgical Transactions A 13 (4) (1982) 627–635.

[29] V. Shrinivas, S. K. Varma, L. E. Murr, Deformation-induced martensitic characteristics in 304 and 316 stainless steels during room-temperature rolling, Metallurgical and Materials Transactions A 26 (3) (1995) 661–671.

[30] K. Staudhammer, L. Murr, S. Hecker, Nucleation and evolution of strain-induced martensitic (b.c.c.) embryos and substructure in stainless steel: A transmission electron microscope study, Acta Metallurgica 31 (2) (1983) 267–274.

[31] F. Badkoobeh, H. Mostaan, M. Rafiei, H. R. Bakhsheshi-Rad, F. Berto, Microstructural characteristics and strengthening mechanisms of ferritic–martensitic dual-phase steels: A review, Metals 12 (1) (2022) 101.

[32] Y. Najafi, Y. Mazaheri, Z. D. Ragheb, H. Daiy, Multi-stage strain-hardening behavior of dual-phase steels: A review, Journal of Materials Research and Technology 31 (2024) 3860–3882.

[33] G. Olson, M. Cohen, Kinetics of strain-induced martensitic nucleation, Metall. Trans. A 6 (1975) 791–795.

[34] M. Soleimani, A. Kalhor, H. Mirzadeh, Transformation-induced plasticity (trip) in advanced steels: A review, Materials Science and Engineering: A 795 (2020) 140023.

[35] L. Janke, C. Czaderski, M. Motavalli, J. Ruth, Applications of shape memory alloys in civil engineering structures—overview, limits and new ideas, Materials and Structures 38 (5) (2005) 578–592.

[36] C. Lauhoff, S. Degener, A. Bolender, A. Liehr, L. Hübner, J. M. Frenck, A. Molotnikov, T. Niendorf, In situ synchrotron diffraction assessment of reversibility of the martensitic transformation in single-crystalline co–ni–ga shape memory alloy under torsion, Shape Memory and Superelasticity 10 (3) (2024) 326–333.

[37] I. Nikitin, B. Scholtes, H. Maier, I. Altenberger, High temperature fatigue behavior and residual stress stability of laser-shock peened and deep rolled austenitic steel aisi 304, Scripta Materialia 50 (10) (2004) 1345–1350.

[38] M. Milad, N. Zreiba, F. Elhalouani, C. Baradai, The effect of cold work on structure and properties of aisi 304 stainless steel, Journal of Materials Processing Technology 203 (1) (2008) 80–85.

[39] C. Ye, S. Suslov, D. Lin, G. J. C. and, Deformation-induced martensite and nanotwins by cryogenic laser shock peening of aisi 304 stainless steel and the effects on mechanical properties, Philosophical Magazine 92 (11) (2012) 1369–1389.

[40] R. Guiheux, S. Berveiller, R. Kubler, D. Bouscaud, E. Patoor, Q. Puydt, Martensitic transformation induced by single shot peening in a metastable austenitic stainless steel 301ln: Experiments and numerical simulation, Journal of Materials Processing Technology 249 (2017) 339–349.

[41] K. Li, W. Yu, Y. Li, H. Bao, Y. Cao, Y. Wang, Study on the effects of laser shock peening on the microstructure and properties of 17-7ph stainless steel, Frontiers in Materials 11 (2024) 1484698.

[42] R. D. Tamiridi, R. Goud, P. Subramaniyan, K. Sivaperuman, A. K. Subramaniyan, I. Charit, S. Gollapudi, Contrasting effects of laser shock peening on austenite and martensite phase distribution and hardness of nitinol, Crystals 12 (9) (2022) 1319.

[43] C. G. Lee, S.-J. Kim, T.-H. Lee, S. Lee, Effects of volume fraction and stability of retained austenite on formability in a 0.1c–1.5si–1.5mn–0.5cu trip-aided cold-rolled steel sheet, Materials Science and Engineering: A 371 (1) (2004) 16–23.

[44] H. Takuda, K. Mori, T. Masachika, E. Yamazaki, Y. Watanabe, Finite element analysis of the formability of an austenitic stainless steel sheet in

warm deep drawing, Journal of Materials Processing Technology 143-144 (2003) 242–248.

[45] H. Hallberg, L. Banks-Sills, M. Ristinmaa, Crack tip transformation zones in austenitic stainless steel, Engineering Fracture Mechanics 79 (2012) 266–280.

[46] R. Eckner, L. Krüger, C. Ullrich, M. Wendler, O. Volkova, Fracture toughness of high-alloy austenitic-martensitic trip steels after q&p processing, International Journal of Fracture 215 (1) (2019) 139–151.

[47] N. S. Ottosen, M. Ristinmaa, The Mechanics of Constitutive Modeling, Elsevier, 2005.

[48] J. Chaboche, Constitutive equations for cyclic plasticity and cyclic viscoplasticity, International Journal of Plasticity 5 (3) (1989) 247–302.

[49] M. F. Horstemeyer, D. J. Bammann, Historical review of internal state variable theory for inelasticity, International Journal of Plasticity 26 (9) (2010) 1310–1334.

[50] J. Lemaitre, Coupled elasto-plasticity and damage constitutive equations, Computer Methods in Applied Mechanics and Engineering 51 (1) (1985) 31–49.

[51] N. Guo, X. Ji, B. Tang, J. Wang, Strain-rate-dependent dislocation-martensite interactions in fe-mn-al-nb medium manganese steel via discrete dislocation dynamics modeling, Materials & Design 263 (2026) 115586.

[52] X. Ou, Molecular dynamics simulations of fcc-to-bcc transformation in pure iron: a review, Materials Science and Technology 33 (7) (2017) 822–835.

[53] F. Roters, P. Eisenlohr, L. Hantcherli, D. Tjahjanto, T. Bieler, D. Raabe, Overview of constitutive laws, kinematics, homogenization and multiscale methods in crystal plasticity finite-element modeling: Theory, experiments, applications, Acta Materialia 58 (4) (2010) 1152–1211.

[54] G. Taylor, Plastic strain in metals, Journal of the Institute of Metals 62 (1938) 307 –324.

[55] J. Rice, Inelastic constitutive relations for solids: An internal-variable theory and its application to metal plasticity, Journal of the Mechanics and Physics of Solids 19 (6) (1971) 433–455.

[56] K. Nguyen, M. Zhang, V. J. Amores, M. A. Sanz, F. J. Montáns, Computational modeling of dislocation slip mechanisms in crystal plasticity: A short review, Crystals 11 (2021) 42.

[57] H. Ji, Q. Song, M. GUPTA, W. Cai, Z. Youle, L. Zhanqiang, Grain scale modelling and parameter calibration methods in crystal plasticity finite element researches: a short review, Journal of Advanced Manufacturing Science and Technology 1 (2021) 41–50.

[58] X. Wang, W. Wu, M. Zhan, Z. Zheng, Z. Li, T. Liu, Analysis of the texture evolution during multipass tube spinning of a ta15 alloy using the crystal plasticity finite element model, Journal of Materials Research and Technology 27 (2023) 6438–6447.

[59] P. Sadowski, M. Rezaee-Hajidehi, S. Stupkiewicz, Deformation twinning as a displacive transformation: computational aspects of the phase-field model coupled with crystal plasticity, Computational Mechanics 77 (1) (2026) 71–95.

[60] H. Salama, O. Shchyglo, I. Steinbach, The interplay between the martensitic transformation rate and the rate of plastic relaxation during martensitic transformation in low-carbon steel, a phase-field study, npj Computational Materials 11 (1) (2025) 43.

[61] M. Wallin, M. Ristinmaa, Finite strain topology optimization based on phase-field regularization, Structural and Multidisciplinary Optimization 51 (2) (2015) 305–317.

[62] G. A. Holzapfel, Nonlinear Solid Mechanics: A Continuum Approach for Engineering, John Wiley & Sons, 2000.

[63] H. Hallberg, P. Håkansson, M. Ristinmaa, A constitutive model for the formation of martensite in austenitic steels under large strain plasticity, International Journal of Plasticity 23 (7) (2007) 1213–1239.

[64] H. Hallberg, P. Håkansson, M. Ristinmaa, Thermo-mechanically coupled model of diffusionless phase transformation in austenitic steel, International Journal of Solids and Structures 47 (11) (2010) 1580–1591.

[65] P. Håkansson, M. Wallin, M. Ristinmaa, Prediction of stored energy in polycrystalline materials during cyclic loading, International Journal of Solids and Structures 45 (6) (2008) 1570–1586.

[66] M. Zhang, K. Nguyen, J. Segurado, F. J. Montáns, A multiplicative finite strain crystal plasticity formulation based on additive elastic corrector rates:

Theory and numerical implementation, International Journal of Plasticity 137 (2021) 102899.

[67] H. M. Asadkandi, T. Mánik, B. Holmedal, O. S. Hopperstad, Open-source implementations and comparison of explicit and implicit crystal-plasticity finite element methods, Computers & Structures 307 (2025) 107621.

[68] J. Gu, X. Chen, J.-H. Jung, Explicit radial basis function runge–kutta methods, Numerical Algorithms (2025) 1.

[69] P. Areias, C. dos Santos, R. Melicio, N. Silvestre, An implicit staggered algorithm for cpfem-based analysis of aluminum, Journal of Theoretical, Computational and Applied Mechanics (2024) 2726–6141.

[70] F. Aldakheel, P. Wriggers, C. Miehe, A modified gurson-type plasticity model at finite strains: formulation, numerical analysis and phase-field coupling, Computational Mechanics 62 (4) (2018) 815–833.

[71] Z. Feng, R. Pokharel, S. C. Vogel, R. A. Lebensohn, D. Pagan, E. Zepeda-Alarcon, B. Clausen, R. Martinez, G. T. Gray, M. Knezevic, Crystal plasticity modeling of strain-induced martensitic transformations to predict strain rate and temperature sensitive behavior of 304 l steels: Applications to tension, compression, torsion, and impact, International Journal of Plasticity 156 (2022) 103367.

[72] J. Park, Y. Hou, J. Min, Z. Hou, H. N. Han, B. He, M.-G. Lee, Understanding plasticity in multiphase quenching & partitioning steels: Insights from crystal plasticity with stress state-dependent martensitic transformation, International Journal of Plasticity 180 (2024) 104075.

[73] K. Veasna, Z. Feng, Q. Zhang, M. Knezevic, Machine learning-based multi-objective optimization for efficient identification of crystal plasticity model parameters, Computer Methods in Applied Mechanics and Engineering 403 (2023) 115740.

[74] S. Lu, X. Zhang, Y. Hu, J. Chu, Q. Kan, G. Kang, Machine learning-based constitutive parameter identification for crystal plasticity models, Mechanics of Materials 203 (2025) 105263.